CrossMark

JFM PAPERS

Hydraulic jump on the surface of a cone

Guangzhao Zhou[1,‡] **and Andrea Prosperetti**[1,2,3,†]

[1]Department of Mechanical Engineering, University of Houston, Houston, TX 77204, USA

[2]Faculty of Science and Technology, and J. M. Burgers Center for Fluid Dynamics, University of Twente, 7500 AE Enschede, The Netherlands

[3]Department of Mechanical Engineering, Johns Hopkins University, Baltimore, MD 21218, USA

This paper addresses several aspects of the axisymmetric flow of a liquid film over the surface of a downward-sloping cone. The study is rooted on a validated computational tool the results of which are interpreted with the help of a hyperbolic time-dependent reduced-order model also derived in the paper. The steady version of the model demonstrates the weakening and ultimate disappearance of the circular hydraulic jump as the cone surface transitions from planar to downward sloping. Mathematically, this evolution is reflected in a change of the model's critical point from spiral to node. A significant advantage of the time-dependent model is that, when it is integrated in time, the flow regions upstream and downstream of the critical point are connected. Due to this feature, when a hydraulic jump exists, its position can be sharply captured automatically with a good agreement with Navier–Stokes simulations. Surface-tension effects are properly accounted for and, in steady conditions, are shown to have a marginal effect on the flow, including the position of the hydraulic jump. A correlation is obtained for the jump radius as a function of the flow rate, liquid viscosity, gravitational acceleration and the angle of inclination of the cone surface. In a suitable limit, the model reduces to the optimal two-dimensional, first-order model for liquid film flow down an inclined plane and, in a different limit, it describes an axisymmetric thin liquid film falling down the surface of a vertical cylinder. Some results are also presented for the waves induced by a pulsating jet on the surface of the liquid film and for a jet impinging on the surface of a cone from below.

Key words: thin films, coating

† Email address for correspondence: aprosper@central.uh.edu
‡ Present address: School of Engineering Science, University of Chinese Academy of Sciences, Beijing 101408, PR China.

1. Introduction

The circular hydraulic jump produced by a liquid jet normally impinging on a flat surface is a commonly observable phenomenon the detailed nature of which, however, has only reluctantly yielded its secrets. The first analyses including the liquid viscosity were carried out by Kurihara (1946) and Tani (1949) who based their studies on the boundary-layer approximation of the Navier–Stokes (NS) equations with a hydrostatic pressure gradient. They derived a reduced-order model which had a critical point approaching which the slope of the free surface diverged. Concerning this prediction, Tani writes 'Actually, however, before reaching the infinite slope, the increase in pressure gradient produces separation of flow from the wall and consequently back flow, thus giving explanation for the sudden thickening of the stream'. This association of the position of the critical point with that of the hydraulic jump was supported by the study of Bohr, Dimon & Putkaradze (1993) and further strengthened by the subsequent work of this group (Bohr, Putkaradze & Watanabe 1997; Bohr *et al.* 1998; Watanabe, Putkaradze & Bohr 2003) and others (see e.g. Fernandez-Feria, Sanmiguel-Rojas & Benilov 2019; Wang & Khayat 2019). There is no need to recapitulate here the history of research on the circular hydraulic jump, which is adequately summarized in several recent papers (see e.g. Mohajer & Li 2015; Askarizadeh *et al.* 2019; Wang & Khayat 2019, 2021; De Vita *et al.* 2020). Suffice it to say that the issue, nature and avoidance of the critical point of the many reduced-order models developed throughout this history have been constant concerns of researchers on this topic.

In the present study we focus on the formation – and disappearance – of the circular hydraulic jump when the solid surface on which the jet impinges is the downward-sloping surface of a cone, of which a horizontal flat plate represents a special case. While our study is primarily based on validated Navier–Stokes numerical simulations, we also develop a hyperbolic time-dependent reduced-order model in which the disappearance of the hydraulic jump is associated with the transition of the nature of a critical point from spiral to node at a critical angle.

Similarly to many others, our reduced-order model is axisymmetric but, unlike others, it is obtained by a Galerkin method patterned after the approach pioneered by Ruyer-Quil & Manneville (2000) for the two-dimensional case. As such, it is the only model that reduces to the optimal two-dimensional model (Kalliadasis *et al.* 2012, p. 168) in the appropriate limit.

We demonstrate a stable and fairly accurate method for the numerical solution of the time-dependent reduced-order model with and without surface tension. Integration to steady state produces a solution of the time-independent version of the model which avoids the difficulties encountered if the solution of this version of the model is tackled directly, a difficulty common to all other steady models in existence. In this way we are able to show how surface tension smoothens the effect of the critical point of the first-order model and, at steady state, produces a smooth free-surface profile in reasonable agreement with the numerical integration of the full Navier–Stokes equations.

Other than for a paper by Bush & Aristoff (2003) and a brief mention in Mathur *et al.* (2007), surface tension has not featured prominently in theoretical studies of the circular hydraulic jump, but it has become a controversial topic (see e.g. Duchesne, Andersen & Bohr 2019) after the paper by Bhagat *et al.* (2018) who make it the crucial parameter for hydraulic jumps, with gravity playing a minor role. The contention of Bhagat, Wilson & Linden (2020) is that this applies not only to developing jumps, for which surface tension and the associated contact angle may be expected to be important near the advancing contact line (Askarizadeh *et al.* 2019; Duchesne & Limat 2022), but also to a wide class of developed jumps. While the arguments put forward by Bhagat *et al.* (2018), Bhagat &

Linden (2020) and Bhagat *et al.* (2020) have been questioned (Duchesne *et al.* 2019), the experimental evidence they presented cannot be ignored and suggests that things go as if gravity were not important. A possible explanation has been suggested in Duchesne & Limat (2022) but more work is needed for a complete resolution of this issue.

Our results refer primarily to the developed case and they imply that the position and structure of the steady jump are little affected by surface tension. When the jet impinges the cone from below, a few examples of which we also briefly consider, the liquid film progresses along the solid surface only up to a point where it detaches and starts to fall. In this case, therefore, the transient dynamics before steady conditions are reached includes a moving contact line and surface tension affects the position at which the film detaches as expected.

Film flow on the outer surface of a cone away from the cone axis is a problem of fluid-mechanical interest in itself on which the literature is surprisingly limited. There is a two-page paper by Scholle, Marner & Gaskell (2019) in which inertia is neglected and the focus is more on the method of analysis than on the results, but the most significant studies on the topic are by Zollars & Krantz (1976, 1980). In the first paper Zollars & Krantz developed an expression for the steady film thickness by a method so involved that they could not describe it in detail. In the present paper we show how the same result can be obtained by a much simpler procedure. In the second paper they studied waves on the surface of a film flowing down a cone in connection with the stability of the steady solution of the first paper. We present limited results on the time-dependent problem by considering the flow induced by a sinusoidally pulsating jet impinging on the cone and show that our reduced-order time-dependent model reproduces the results of Navier–Stokes simulations with good accuracy.

In the next section we introduce the geometry to be studied and the governing equations. Two alternative scalings of the equations, based on the assumption that the film is thin compared with the relevant scale in the flow direction, are described in § 3 where a simplified formulation able to deal with both is developed. This simplified formulation is used in § 4 to derive the reduced-order model. Sections 5 and 7 are devoted to a study of the model and to a comparison with Navier–Stokes simulations. The numerical set-up for the integration of the Navier–Stokes equations is described in § 6 and Appendix C. The time-dependent version of the model is taken up in §§ 8 and 10, where it is compared with numerical solutions of the Navier–Stokes equations for the case of a pulsating jet. The role of surface tension is addressed in § 9 and further explored for an upward-directed jet in § 11. The model can be readily adapted to the case of a two-dimensional film flowing down an inclined plate, a problem studied by several authors in connection with the formation of hydraulic jumps in this type of flows (Higuera 1994; Singha, Bhattacharjee & Ray 2005; Dasgupta & Govindarajan 2010; Dasgupta, Tomar & Govindarajan 2015; Dhar, Das & Das 2020). We briefly comment on this work in § 12. Another interesting limit, taken up in Appendix B, is the flow of a liquid film on the surface of a circular cylinder (see e.g. Frenkel 1992; Kalliadasis & Chang 1994; Ruyer-Quil *et al.* 2008; Ding & Wong 2017; Ji *et al.* 2019).

A different class of problems related to the flow on the surface of a cone concerns flows directed toward, rather than away from, the cone axis, as on the inner surface of a funnel (see e.g. Al-Hawaj 1999; Lin, Dijksman & Kondic 2021; Xue & Stone 2021). Such problems are inherently transient and require an analysis of the advancing contact line. They are not addressed in the present work. Another related problem is the flow on the underside of a conical surface, which exhibits Rayleigh–Taylor instabilities similar to those investigated in the case of spherical surfaces (see e.g. Balestra, Nguyen & Gallaire 2018). We only make a very brief mention of this problem in § 11.
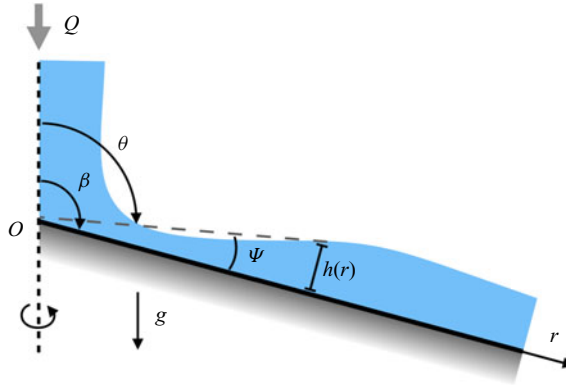
Figure 1. Geometry and coordinate system used in this paper; r and θ are the spherical polar coordinates centred at the vertex of the cone with downward aperture $2(\pi - \beta)$; $\Psi = \Psi(r, t)$ and $h = h(r, t)$ are the angular and actual heights of the film surface above the cone surface.

2. Coordinate system and governing equations

We adopt a standard spherical polar coordinate system taking the upward-directed axis of the cone as the polar axis (figure 1). The origin is placed at the cone tip; the distance from the origin is denoted by r and the polar angle measured from the positive half of the polar axis by θ. The surface of the cone is identified by $\theta = \beta$. A cone extending downward below the origin has $\beta > \pi/2$; for $\beta = \pi/2$, the cone surface degenerates into a horizontal plane. The polar angle of the film free surface is $\beta + \Psi(r, t)$ so that, for a film flowing over the cone surface, $\Psi < 0$. It is convenient to introduce the reduced angular coordinate

$$\psi = \theta - \beta, \tag{2.1}$$

so that the film occupies the region $\Psi(r, t) \leqslant \psi \leqslant 0$ and its surface is located at $\psi = \Psi$.

The height of the film measured normally to the local cone surface is denoted by $h(r, t)$. It can be easily shown that the difference between h and the arc length $r(-\Psi)$ is of order h^2/r^2, i.e. of second order of smallness in the parameter ϵ to be defined shortly. Since the theory to be presented is accurate to first order in ϵ, this small difference can be neglected. Thus, in the following, we set $h(r, t) = -r\Psi(r, t)$.

In spherical polar coordinates the equation of continuity is

$$\frac{1}{r^2}\partial_r(r^2 u) + \frac{1}{r\sin\theta}\partial_\theta(\sin\theta v) = 0, \tag{2.2}$$

with u and v the velocity components in the radial and angular directions and $v > 0$ when the velocity is directed toward the cone surface. The θ- and r-momentum equations are

$$\partial_t v + u\partial_r v + \frac{v}{r}\partial_\theta v + \frac{uv}{r} = -\frac{1}{\rho r}\partial_\theta p + g\sin\theta$$
$$+ \nu\left[\frac{1}{r}\partial_r^2(rv) + \frac{1}{r^2}\partial_\theta^2 v + \frac{\cot\theta}{r^2}\partial_\theta v + \frac{2}{r^2}\partial_\theta u - \frac{v}{r^2\sin^2\theta}\right], \tag{2.3}$$

951 A20-4

and

$$\partial_t u + u \partial_r u + \frac{v}{r} \partial_\theta u - \frac{v^2}{r}$$
$$= -\frac{1}{\rho} \partial_r p - g \cos\theta + \nu \left[\frac{1}{r} \partial_r^2 (ru) + \frac{1}{r^2} \partial_\theta^2 u + \frac{\cot\theta}{r^2} \partial_\theta u - \frac{2}{r^2} \partial_\theta v - \frac{2}{r^2} u - \frac{2\cot\theta}{r^2} v \right],$$
(2.4)

respectively. Here, p is the pressure, g the acceleration due to gravity (positive downward) and ρ and ν are the liquid density and kinematic viscosity, respectively.

At the free surface $\psi - \Psi(r, t) = 0$ the kinematic condition stipulates that

$$r \partial_t \Psi = [v]_s - r[u]_s \partial_r \Psi,$$
(2.5)

in which the subscript s denotes evaluation at the free surface. Proceeding in a standard way, we now multiply (2.2) by $r^2 \sin\theta \, d\theta = r^2 \sin\theta \, d\psi$ and integrate from $\psi = 0$ to $\psi = \Psi$ to find

$$\partial_r \left(r^2 \int_0^\Psi \sin\theta u \, d\psi \right) - r \sin(\beta + \Psi) \left(r[u]_s \partial_r \Psi - [v]_s \right) = 0.$$
(2.6)

The first term is proportional to the volumetric flow rate Q in the film,

$$q(r, t) \equiv \frac{Q}{2\pi} = -r^2 \int_0^\Psi \sin\theta u \, d\psi,$$
(2.7)

while the last two terms can be expressed in terms of $\partial_t \Psi$ from (2.5). The result is, with $h = r(-\Psi)$,

$$\partial_t h + \frac{1}{r \sin(\beta - h/r)} \partial_r q = 0,$$
(2.8)

which is the standard relation expressing the time derivative of the film height as the divergence of the volumetric flow rate (see e.g. Oron, Davis & Bankoff 1997; Leal 2007). We have introduced a minus sign in the definition (2.7) of Q to compensate for the fact that, here, $\Psi < 0$ as noted before. As defined, therefore, $Q > 0$ when the flow is directed away from axis of the cone.

3. Scalings

The existing theories for the circular hydraulic jump make use of the boundary-layer approximation of the Navier–Stokes equations according to which inertia, pressure gradient and the part of the Laplacian normal to the boundary are of similar order (see e.g. Watson 1964; Watanabe *et al.* 2003). On the other hand, modelling of the flow down an inclined surface is usually carried out in the framework of what may be called the Kapitza scaling in which, to leading order, the streamwise component of gravity is primarily balanced by the normal Laplacian, inertia and pressure being of small order (see e.g. Kalliadasis *et al.* 2012). The problem to be addressed here shares features of both situations, with the boundary-layer scaling relevant in the region of the hydraulic jump and the Kapitza scaling in the lower-velocity region downstream of the jump. We now consider these two situations and show that a single approximate form of the equations can be used for both situations as long as second-order errors are acceptable.

We start by scaling the coordinates and the dependent variables in a general way according to

$$t \to \frac{Lt}{U}, \quad r \to Lr, \quad \psi \to \frac{\delta}{L}\psi, \quad u \to Uu, \quad v \to Vv, \quad p \to \Delta P p, \quad (3.1a\text{-}f)$$

in which the velocity and pressure scales U, V and ΔP will be specified as appropriate for each scaling, δ is of the order of the film thickness and L is a characteristic length for the radial variable, assumed to be much larger than δ. Upon substituting into the equation of continuity we find the familiar result

$$\frac{V}{U} = \frac{\delta}{L} \equiv \epsilon, \quad (3.2)$$

with $\epsilon \ll 1$. Since $\partial_\theta = \partial_\psi$, $\partial_\theta \to (1/\epsilon)\partial_\psi$ and the scaled equations become

$$\frac{1}{r^2}\partial_r(r^2 u) + \frac{1}{r}\partial_\psi v + \epsilon \frac{\cot\theta}{r} v = 0, \quad (3.3)$$

$$\epsilon^2 \left(\partial_t v + u\partial_r v + \frac{v}{r}\partial_\psi v + \frac{uv}{r} \right)$$

$$= -\frac{\Delta P}{\rho U^2 r}\partial_\psi p + \epsilon \frac{Lg}{U^2}\sin\theta$$

$$+ \frac{v}{LU}\left[\epsilon^2 \frac{1}{r}\partial_r^2(rv) + \frac{1}{r^2}\partial_\psi^2 v + \frac{\epsilon\cot\theta}{r^2}\partial_\psi v + \frac{2}{r^2}\partial_\psi u - \epsilon^2 \frac{v}{r^2\sin^2\theta} \right], \quad (3.4)$$

and

$$\epsilon^2 \left(\partial_t u + u\partial_r u + \frac{v}{r}\partial_\psi u - \epsilon^2 \frac{v^2}{r} \right)$$

$$= -\epsilon^2 \frac{\Delta P}{\rho U^2}\partial_r p - \epsilon^2 \frac{Lg}{U^2}\cos\theta$$

$$+ \frac{v}{LU}\left[\epsilon^2 \frac{1}{r}\partial_r^2(ru) + \frac{1}{r^2}\partial_\psi^2 u + \epsilon \frac{\cot\theta}{r^2}\partial_\psi u - \epsilon^2 \frac{2}{r^2}\partial_\psi v - \frac{2\epsilon^2}{r^2}u - 2\epsilon^3 \frac{\cot\theta}{r^2}v \right]. \quad (3.5)$$

As long as ϵ is small, the terms multiplied by ϵ^2 and ϵ^3 in the viscous contributions on the right-hand side of these equations will always be small compared with the other ones and can be dropped. Furthermore, since $|\psi| \sim h/r \sim \epsilon$, terms proportional to $\epsilon\cot\theta$ can be replaced by $\epsilon\cot\beta$ with an $O(\epsilon^2)$ error. The same approximation can be applied to the equation of continuity which then becomes

$$\frac{1}{r^2}\partial_r(r^2 u) + \frac{1}{r}\partial_\psi v + \epsilon \frac{\cot\beta}{r} v = 0. \quad (3.6)$$

For the Kapitza scaling we let

$$U = \frac{g\delta^2}{\nu}, \quad \Delta P = \rho g\delta. \quad (3.7a,b)$$

Up to a numerical factor, the velocity scale is of the order of the mean Nusselt velocity for the flow of a flat film down a vertical solid plane while the pressure scale expresses the dominance of hydrostatic effects. In principle these scales should be adjusted according to

951 A20-6

the inclination of the solid surface but, here, the aperture of the cone is an important parameter which should not be hidden in the normalization. With these choices, the equation of continuity maintains the form (3.6) and the ψ (or θ) momentum equation becomes

$$\epsilon^2 \left(\partial_t v + u \partial_r v + \frac{v}{r} \partial_\psi v + \frac{uv}{r} \right) = -\frac{v^2}{g\delta^3} \left(\frac{1}{r} \partial_\psi p - \sin\theta \right)$$
$$+ \epsilon \frac{v^2}{g\delta^3} \frac{1}{r^2} \left(\partial_\psi^2 v + 2\partial_\psi u + \epsilon \cot\beta \, \partial_\psi v \right). \quad (3.8)$$

This equation explicitly shows the dominant balance of gravity and pressure gradient normal to the solid surface, with viscous effects minor and inertia of secondary importance. After division by ϵ, the r momentum equation becomes

$$\epsilon \left(\partial_t u + u \partial_r u + \frac{v}{r} \partial_\psi u \right) = -\frac{v^2}{g\delta^3} \left(\cos\theta + \epsilon \partial_r p \right) + \frac{v^2}{g\delta^3} \frac{1}{r^2} \left(\partial_\psi^2 u + \epsilon \cot\beta \, \partial_\psi u \right). \quad (3.9)$$

The dimensionless group $g\delta^3/v^2$ can be written as $\delta U/v$ and is seen therefore to play the role of a Reynolds number based on the film thickness. In order to reflect, to leading order, the dominant balance between streamwise gravity and viscosity characteristic of film flow down an inclined plane, it is evident that this Reynolds number must be of order 1 or smaller.

For the boundary-layer scaling we assume that the velocity scale U is imposed by some external agent, such as the jet that causes the hydraulic jump, and that the pressure scale is $\Delta P = \rho U^2$ as in normal boundary-layer theory. The ψ momentum equation becomes

$$\epsilon^2 \left(\partial_t v + u \partial_r v + \frac{v}{r} \partial_\psi v + \frac{uv}{r} \right) = -\frac{1}{r} \partial_\psi p + \frac{1}{Re} \frac{1}{r^2} \left(\partial_\psi^2 v + 2\partial_\psi u + \epsilon \cot\beta \, \partial_\psi v \right)$$
$$+ \frac{\epsilon Lg}{U^2} \sin\theta, \quad (3.10)$$

in which $Re = UL/v$ is the Reynolds number, and the r momentum equation

$$\epsilon^2 Re \left(\partial_t u + u \partial_r u + \frac{v}{r} \partial_\psi u \right) = -\epsilon^2 Re \, \partial_r p + \frac{1}{r^2} \left(\partial_\psi^2 u + \epsilon \cot\beta \, \partial_\psi u \right) - \epsilon^2 Re \frac{Lg}{U^2} \cos\theta. \quad (3.11)$$

The standard form of the boundary-layer equations is recovered upon taking $Re = O(\epsilon^{-2})$. Equation (3.10) shows then that inertial and viscous contributions to the normal pressure gradient are of second order while, in order to have a physically significant balance, it is necessary to assume $Lg/U^2 \sim O(1/\epsilon)$. From this remark, the r-momentum equation then shows that this boundary-layer scaling is only appropriate provided $\cos\theta \sim O(\epsilon)$. This conclusion can be restated in a more interesting way: in order for the streamwise pressure to have the same order of magnitude as inertia and viscosity, which is a necessary condition for the existence of a hydraulic jump, it is necessary that the inclination of the solid surface be small. The results to be presented later will confirm this conclusion.

As already stated, we will work correct to $O(\epsilon)$. Upon dropping all $O(\epsilon^2)$ terms from the Kapitza form of the momentum equations we have (3.9) and

$$-\frac{1}{r} \partial_\psi p + \sin\theta + \frac{\epsilon}{r^2} \left(\partial_\psi^2 v + 2\partial_\psi u \right) = 0, \quad (3.12)$$

while the boundary-layer form becomes, with $\epsilon^2 Re = 1$,

$$-\frac{1}{r}\partial_\psi p + \frac{\epsilon Lg}{U^2}\sin\theta = 0, \tag{3.13}$$

and

$$\partial_t u + u\partial_r u + \frac{v}{r}\partial_\psi u = -\partial_r p + \frac{1}{r^2}\partial_\psi^2 u - \frac{\epsilon Lg}{U^2}\frac{\cos\theta}{\epsilon}. \tag{3.14}$$

In the last equation we have explicitly used the fact that, for consistency, $\epsilon Lg/U^2$ must be of order 1 so that $\cos\theta = \cos(\beta + \psi) = \cos\beta + O(\epsilon)$ must be of order ϵ. This remark also implies that terms proportional to $\epsilon\cot\beta$ in the momentum and continuity equations are of order ϵ^2 and can, therefore be omitted. For the boundary-layer scaling, therefore, the equation of continuity simplifies to

$$\frac{1}{r^2}\partial_r(r^2 u) + \frac{1}{r}\partial_\psi v = 0. \tag{3.15}$$

A consideration of the equations of continuity (3.6) and (3.15) in the two scalings shows that the two differ by the term $\epsilon(\cot\beta)\,v/r$. Only the inertial term in the Kapitza r momentum equation (3.9) is affected if this difference is disregarded but, since this term is of order ϵ, the error thus introduced is of an inconsequential order ϵ^2. The boundary-layer form of the continuity and ψ momentum equations can therefore be used when either scaling is appropriate. On a similar basis, the difference between the pressures in the two scaling arises from the ϵ term in the Kapitza ψ momentum equation (3.12) and enters the r momentum equation (3.9) where the pressure gradient is multiplied by ϵ, thus introducing another negligible contribution of order ϵ^2 if the boundary-layer form (3.13) is used. Furthermore, $\sin\theta = \sin(\beta + \psi) = \sin\beta\cos\psi + \cos\beta\sin\psi = \sin\beta + O(\epsilon)$ with the Kapitza scaling, while $\sin\theta = \sin\beta + O(\epsilon^2)$ with the boundary-layer scaling since $\cos\beta = O(\epsilon)$. Thus, with either scaling, we can consistently approximate (3.12) and (3.13) by

$$-\frac{1}{r}\partial_\psi p + \frac{\epsilon Lg}{U^2}\sin\beta = 0, \tag{3.16}$$

or the equivalent form with the Kapitza scaling. The two radial momentum equations differ by the presence of the term $\epsilon(\cot\beta/r^2)\partial_\psi u$ in the Kapitza form. This term will, however, be of order ϵ^2 and, therefore, negligible when the boundary-layer scaling is appropriate and it can therefore be retained without significant error. Thus we conclude that a mathematical model consistent with both scalings can be built from the continuity and ψ momentum equations of the boundary-layer scaling, together with the r momentum equation of the Kapitza scaling.

Returning to the unscaled form, therefore, the equations to be considered are (3.15) and

$$-\frac{1}{r}\partial_\psi p + \rho g\sin\beta = 0, \tag{3.17}$$

and

$$\partial_t u + u\partial_r u + \frac{v}{r}\partial_\psi u = -\frac{1}{\rho}\partial_r p + \frac{v}{r^2}\left(\partial_\psi^2 u + \cot\beta\,\partial_\psi u\right) - g\cos\theta. \tag{3.18}$$

In the language of singular perturbations theory we can describe the previous analysis and conclusion by stating that the Kapitza and boundary-layer scalings are two distinguished limits of the scaled equations (3.4) and (3.5). The final system with which we will be concerned, namely (3.15), (3.17) and (3.18), is then the set of composite equations valid in both distinguished limits according to the extension theorem of singular perturbation theory (see e.g. Lagerstrom & Casten 1972).

3.1. *Boundary conditions*

With the free surface defined by $\psi - \Psi(r, t) = 0$ as before, the unit normal is given by

$$n = \frac{-r\partial_r\Psi e_r + e_\theta}{\sqrt{1 + (r\partial_r\Psi)^2}} \simeq -r\partial_r\Psi e_r + e_\theta, \qquad (3.19)$$

with e_r and e_θ unit vectors in the coordinate directions. Consistent to first order in Ψ, the square root in this expression can be approximated by 1, which implies that the slope of the free surface is small so that the last step is accurate to the order of $O(\epsilon)$. As we will see, it is possible that this approximation contributes some error in the neighbourhood of a hydraulic jump on a horizontal surface, but the effect remains localized (see e.g. figure 12). The unit tangent t to the free surface is $t = (e_r, r\partial_r\Psi e_\theta) + O(\epsilon^2)$. The curvature $\mathcal{C}$ of the free surface is approximately given by

$$\mathcal{C} = [\nabla \cdot n]_{\psi=\Psi} \simeq \frac{\cot(\beta + \Psi)}{r} - \frac{1}{r^2}\partial_r(r^3\partial_r\Psi). \qquad (3.20)$$

The two terms are of the same order when $\cot\beta = O(\epsilon)$, but the second one is of order ϵ compared with the first one when $\cot\beta = O(1)$. To $O(\epsilon)$, in terms of h, this equation is

$$\mathcal{C} \simeq \frac{\cot\beta}{r} + \frac{h}{r^2\sin^2\beta} + \frac{1}{r^2}\partial_r\left(r^3\partial_r\frac{h}{r}\right). \qquad (3.21)$$

When the medium above the film has a constant pressure p_a but otherwise negligible dynamical effects, which we assume, the dynamic condition requires that the stress tangent to the free surface vanishes. It is readily shown that, correct to $O(\epsilon)$, this condition simply implies that

$$\frac{1}{r}\partial_\psi u = 0, \qquad (3.22)$$

which is a standard condition in thin-film analysis (see e.g. Bohr *et al.* 1993; Oron *et al.* 1997; Ruyer-Quil & Manneville 1998, 2000; Watanabe *et al.* 2003). With $\mathcal{C}^* = L\mathcal{C}$, for the Kapitza scaling, the dynamic condition on the normal stress can be written as

$$-p^* + 2\epsilon\left(\frac{1}{r^*}\partial_{\psi^*}v^* + \frac{u^*}{r^*} - \partial_{r^*}\Psi^*\partial_{\psi^*}u^*\right) = -p_a^* + \frac{\sigma}{\rho g\delta L}\mathcal{C}^*, \qquad (3.23)$$

where σ is the surface-tension coefficient and we temporarily use asterisks to denote normalized variables. According to (3.9), the $O(\epsilon)$ terms give an $O(\epsilon^2)$ contribution to the r momentum equation and are therefore negligible. In order to retain the effect of surface tension it is necessary to assume that $\sigma/(\rho g\delta L) = O(1)$. With the boundary-layer scaling, the condition is

$$-p^* + \frac{2}{Re}\left(\frac{1}{r^*}\partial_{\psi^*}v^* + \frac{u^*}{r^*} - \partial_{r^*}\Psi^*\partial_{\psi^*}u^*\right) = -p_a^* + \frac{\sigma}{\rho U^2 L}\mathcal{C}^*, \qquad (3.24)$$

and, given that $Re = O(\epsilon^{-2})$, the term in parentheses is negligible. Surface tension remains a non-negligible force if $\sigma/(\rho U^2 L) = O(1)$. Thus we see that, for both cases, the normal stress condition reduces to the dimensional form

$$p = p_a - \sigma\mathcal{C}. \qquad (3.25)$$

At the solid surface $\psi = 0$ the no-slip condition applies.

4. Approximate equation for the film thickness

Starting with Tani (1949), several authors have pointed out that, approximately, the location of the hydraulic jump can be determined on the basis of a simplified first-order equation for the film height derived for steady flow. We take a different approach and start by deriving an equation for time-dependent flow reducing it to the steady case at the appropriate moment.

Rather than following the von Kármán–Pohlhausen method used in earlier studies (Tani 1949; Watson 1964; Watanabe *et al.* 2003), in our derivation we adapt to the present situation the Galerkin method developed by Ruyer-Quil & Manneville (1998, 2000) for the two-dimensional case, which has proven very effective in that case. The approximate results to be derived here will be supported by the numerical solutions of the full Navier–Stokes equations.

Upon integrating (3.17) we find

$$p = p_a + \rho g \sin \beta r(\psi - \Psi) - \sigma \mathcal{C}. \tag{4.1}$$

This relation can now be substituted into the *r*-momentum equation (3.18) to find

$$\partial_t u + u \partial_r u + \frac{v}{r} \partial_\psi u = g \sin \beta (\Psi + r \partial_r \Psi) + \frac{\sigma}{\rho} \partial_r \mathcal{C}$$
$$+ \frac{v}{r^2} (\partial_\psi^2 u + \cot \beta \partial_\psi u) - g \cos \beta, \tag{4.2}$$

in which we have expanded $g \cos \theta = g \cos(\beta + \psi)$ correctly to first order in the last term.

We now write the radial velocity in the similarity form used by many earlier authors (see e.g. Watson 1964; Watanabe *et al.* 2003), which, in our case, is

$$u = \frac{\psi}{\Psi} \left(2 - \frac{\psi}{\Psi}\right) V(r, t), \tag{4.3}$$

with the surface radial velocity $V(r, t)$ to be determined by relating u to the volumetric flow rate of the film as shown below. It may be noted that (4.3) satisfies no slip at the wall and zero tangential stress on the free surface as per (3.22). In the spirit of the Galerkin method we multiply (4.2) by u and integrate over the film thickness

$$\int_0^\Psi u \partial_t u \, d\psi + \int_0^\Psi u \left(u \partial_r u + \frac{v}{r} \partial_\psi u\right) d\psi$$
$$= \frac{v}{r^2} \int_0^\Psi u \left(\partial_\psi^2 u + \cot \beta \partial_\psi u\right) d\psi + \left[[\sin \beta \partial_r (r\Psi) - \cos \beta]g + \frac{\sigma}{\rho} \partial_r \mathcal{C}\right] \int_0^\Psi u \, d\psi. \tag{4.4}$$

Use of the equation of continuity in the simplified boundary-layer form (3.15), of the kinematic boundary condition (2.5), of the shear stress condition (3.22) and integration by parts permit us to rewrite the previous equation to gain some physical understanding at the same time simplifying somewhat the calculations

$$\frac{1}{2} \partial_t \int_0^\Psi u^2 \, d\psi + \frac{1}{2r^2} \partial_r \left(r^2 \int_0^\Psi u^3 \, d\psi\right) = \left(g[\sin \beta \partial_r (r\Psi) - \cos \beta] + \frac{\sigma}{\rho} \partial_r \mathcal{C}\right) \int_0^\Psi u \, d\psi$$
$$+ \frac{v}{r^2} \left(-\int_0^\Psi (\partial_\psi u)^2 \, d\psi + \frac{1}{2} \cot \beta [u^2]_s\right). \tag{4.5}$$

To $O(\epsilon)$, this will be recognized as the integral form of the kinetic energy balance for the liquid. The first and second terms on the left-hand side are the rate of change of the kinetic energy and the divergence of the kinetic energy flow rate. On the right-hand side, the first term is the integral of $-\nabla \cdot (pu/\rho) + u \cdot g = u \cdot (-\nabla p/\rho + g)$ and the second one the integral of the dissipation function. Again using $\Psi = -h/r$, after substitution of u by V, integration and multiplication by $-r^2$, the final result may be written as

$$\frac{4}{15}\partial_t\left(rhV^2\right) + \frac{8}{35}\partial_r\left(rhV^3\right)$$
$$= \frac{2}{3}rhV\left[-g(\sin\beta\partial_r h + \cos\beta) + \frac{\sigma}{\rho}\partial_r\mathcal{C}\right] - \frac{4}{3}\nu\frac{r}{h}V^2\left(1 + \frac{3}{8}\cot\beta\frac{h}{r}\right). \quad (4.6)$$

It is convenient to rewrite this equation in terms of the volumetric flow rate $q = Q/2\pi$ because this quantity is a constant in steady conditions. Expanding $\sin\theta$ to first order in the definition (2.7) of q we have

$$q \simeq -r^2\int_0^{\Psi}(\sin\beta + \cos\beta\psi)u\,d\psi = \frac{2}{3}rhV\sin\beta\left(1 - \frac{5}{8}\cot\beta\frac{h}{r}\right), \quad (4.7)$$

from which

$$V = \frac{3q}{2rh\sin\beta}\left[1 + \frac{5}{8}\cot\beta\frac{h}{r} + O\left(\frac{h^2}{r^2}\right)\right]. \quad (4.8)$$

An examination of the order of magnitude of the terms in (4.6) shows that it is consistent to retain the $O(h/r)$ term of this relation only in the viscous term on the right-hand side. Furthermore, the $\partial_t h$ terms can be expressed in terms of the volumetric flux q by using the integrated continuity equation (2.8) which, itself, can be expanded to read

$$\partial_t h + \frac{1}{r\sin\beta}\left(1 + \cot\beta\frac{h}{r}\right)\partial_r q = 0. \quad (4.9)$$

With this step, correct to $O(h/r)$, the integral form (4.6) of the momentum equation becomes

$$\partial_t q + \frac{17}{7}\frac{q}{hr\sin\beta}\partial_r q - \frac{5}{6}\left(\frac{54}{35}\frac{q^2}{h^2 r\sin\beta} - ghr\sin^2\beta\right)\partial_r h$$
$$= -\frac{5}{6}hr\sin\beta\left(g\cos\beta - \frac{\sigma}{\rho}\partial_r\mathcal{C}\right) + \frac{9}{7}\frac{q^2}{hr^2\sin\beta} - \frac{5}{2}\frac{\nu q}{h^2}\left(1 + \cot\beta\frac{h}{r}\right). \quad (4.10)$$

This equation, together with (4.9), or its original form (2.8), which relates the film thickness to the volumetric flow rate, constitutes a two-equation model for the time-dependent evolution of the film.

It is interesting to relate this result to the form derived by Ruyer-Quil & Manneville (2000) for two-dimensional flow down an inclined plate, as this equation has been shown to be optimal at first order (Kalliadasis *et al.* 2012, p. 168). This objective can be achieved by identifying $Q/(2\pi r\sin\beta) = q/(r\sin\beta)$ with the two-dimensional flow rate q_{2D} and by taking the limit $r \to \infty$. The first step is necessary because Q is the flow rate through a circular surface of radius $r\sin\beta$ so that $Q/(2\pi r\sin\beta)$ is the flow rate per unit width. The second one reflects the fact that, as $r \to \infty$, the effect of the cone curvature becomes

smaller and smaller approaching a flat surface. With these steps, after writing x in place of r, (4.9) becomes

$$\partial_t h + \partial_x q_{2D} = 0, \tag{4.11}$$

while (4.10) becomes

$$\partial_t q_{2D} + \frac{17}{7} \frac{q_{2D}}{h} \partial_x q_{2D} - \frac{5}{6} \left(\frac{54}{35} \frac{q_{2D}^2}{h^2} - gh \sin\beta \right) \partial_x h$$

$$= -\frac{5}{6} h \left(g\cos\beta - \frac{\sigma}{\rho} \partial_x \mathcal{C} \right) - \frac{5}{2} \frac{\nu}{h^2} q_{2D}, \tag{4.12}$$

with $\mathcal{C} = \partial_x^2 h$. This is precisely the first-order model for two-dimensional flow of a thin film over an inclined plate derived in Ruyer-Quil & Manneville (2000). In steady conditions $\partial_t h = 0$ so that $\partial_x q_{2D} = 0$ and the second equation becomes

$$\left(\frac{54}{35} \frac{q_{2D}^2}{h^2} - gh\sin\beta \right) \frac{\mathrm{d}h}{\mathrm{d}x} = \left(g\cos\beta - \frac{\sigma}{\rho} \frac{\mathrm{d}\mathcal{C}}{\mathrm{d}x} \right) h + 3 \frac{\nu}{h^2} q_{2D}. \tag{4.13}$$

If the inclination to the horizontal is denoted by η, then $\beta = \frac{\pi}{2} + \eta$ so that $\cos\beta = -\sin\eta$. This equation then possesses a uniform solution in which the film thickness is related to the flow rate according to the well-known Nusselt result (see e.g. Chang & Demekhin 2002; Kalliadasis *et al.* 2012)

$$q_{2D} = \frac{gh^3 \sin\eta}{3\nu}. \tag{4.14}$$

5. First-order equation for steady flow

In steady conditions $\partial_t h = 0$ and $\partial_t q = 0$ so that (4.9) simply states that q is constant. Using this fact in (4.10) and dropping the surface-tension term $\partial_r \mathcal{C}$, we obtain the first-order equation

$$\left(\frac{54}{35} \frac{q^2}{r^2 \sin^2\beta} - gh^3 \sin\beta \right) \frac{\mathrm{d}h}{\mathrm{d}r}$$

$$= h^3 g\cos\beta - \frac{54}{35} \frac{hq^2}{r^3 \sin^2\beta} + \frac{3\nu q}{r\sin\beta} \left(1 + \cot\beta \frac{h}{r} \right). \tag{5.1}$$

For $\beta = \pi/2$ a similar equation has been derived by many authors. In all cases the groups of dimensional terms have the same structure, namely gh^3, q^2/r^2 etc., and they carry the same signs, but the numerical coefficients are different. Since, as already noted, (5.1) reduces to the optimal two-dimensional equation in the appropriate limit, we believe that our coefficients are preferable. There is only one previous study which includes a small deviation of the plate from planarity (Kasimov 2008). In that study the equation analogous to (5.1) is written as

$$\left(\frac{6q^2}{5r^2} - gh^3 \right) \frac{\mathrm{d}h}{\mathrm{d}r} = s_b gh^3 + \frac{3\nu q}{r} - \frac{6q^2 h}{5r^3}, \tag{5.2}$$

in which s_b is the plate slope, assumed to be small; in our notation, $s_b = \tan(\pi/2 - \beta)$. For angles close to $90°$ this equals $\sin(\pi/2 - \beta) = \cos\beta$ and $\sin\beta \simeq 1$, so that (5.2) and

951 A20-12

(5.1) agree in this limit of small inclination except for the coefficient $\frac{54}{35} \simeq 1.543$ replacing $\frac{6}{5} = 1.2$.

For future reference it may be pointed out that, for large r, (5.1) has the approximate solution

$$h \simeq \left(\frac{3\nu q}{g \sin \beta (- \cos \beta) r} \right)^{1/3}, \tag{5.3}$$

in agreement with the result of Zollars & Krantz (1980). We have verified that the additional terms that we can calculate from (5.1) agree with those given in Zollars & Krantz (1980). Since the method used by these authors is very different from the present one, agreement of the present results with the numerical coefficients that they found lends further support to the correctness of our derivation.

The expression (5.3) may be considered as the three-dimensional analogue of the Nusselt solution (4.14) and describes a situation in which gravity balances viscosity even though the film thins by continuity due to the diverging nature of the cone surface area. It is evident that (5.3) becomes meaningless as $\cos \beta \to 0$ as, in that case, gravity cannot assist in generating a flow of the film. The absence of an asymptotic solution of equations of the form (5.1) for $\beta = 90°$ has been proven and discussed earlier in Bohr *et al.* (1993).

6. Conditions for the numerical simulations

The direct numerical simulations are carried out with the open-source software OpenFOAM v2012, as described in Appendix C. These simulations require a boundary condition at the right end of the domain. In order to minimize the effect of these conditions on the steady-state solution in which we are mostly interested, following Fernandez-Feria *et al.* (2019) and Wang & Khayat (2021), we simulate the free fall of the film down a vertical solid surface attached to the end of the inclined cone surface, as shown in figure 15.

Figure 2 compares our predictions of the hydraulic jump phenomenon against the experimental data by Duchesne *et al.* (2014). Silicon oil (with density 960 kg m^{-3}, kinematic viscosity 2×10^{-5} m^2 s^{-1} and surface-tension coefficient 0.02 N m^{-1}) is injected downward from a 1.6 mm-radius round nozzle onto a horizontally placed circular disk with a radius of 15 cm. The volumetric flow rate is 17 cm^3 s^{-1}. The inlet is placed 4.8 mm above the plate. As shown in Brechet & Néda (1999), this nozzle-to-wall distance has little influence on the position of the hydraulic jump. One observes a close agreement between experiment and simulations, which supports the accuracy of the latter.

Figure 3 shows a comparison of our numerical results for different jet flow rates Q (closed circles and squares) with some experiments of Hansen *et al.* (1997) for water (open circles) and an oil with a kinematic viscosity 15 times that of water (open squares). The solid lines are the predictions of the inertial lubrication theory of Rojas *et al.* (2010) while the dashed lines are just guides to the eyes. The agreement with the oil data is quite good. That with the water data less so, although our results are in very close agreement with those of Rojas *et al.* (2010). It may also be noted that Hansen *et al.* (1997) state that the radius of the jump was oscillating for Q greater than approximately 15 cm^3 s^{-1} so that the data shown are mean values. Since the unsteadiness mentioned by Hansen *et al.* was not observed in our simulation, it is possible that it was caused by the specific experimental system used. Some additional considerations on this comparison can be found in the supplementary material associated with this paper available at https://doi.org/10.1017/jfm. 2022.777.

Finally, a comparison with the numerical results of Fernandez-Feria *et al.* (2019), included in Appendix C, is in excellent agreement with the reported results.
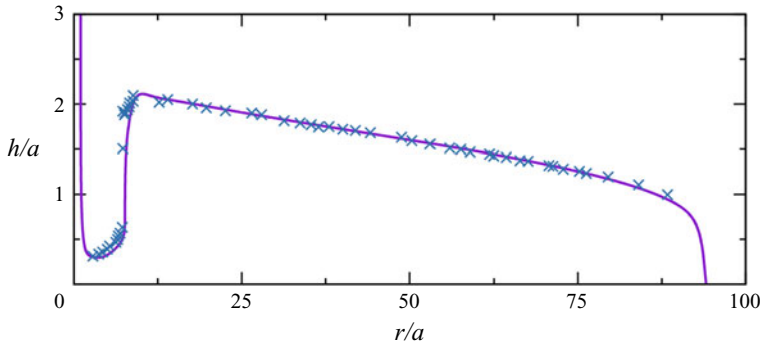
Figure 2. Comparison of the free-surface profile normalized by the jet radius, h/a, as given by the present Navier–Stokes simulations (solid line) with the data of Duchesne, Lebon & Limat (2014) (symbols).
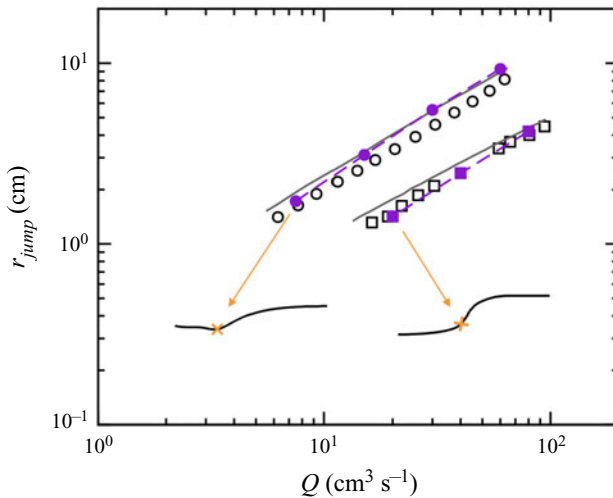

Figure 3. Comparison of our Navier–Stokes simulations (solid symbols) for the jump radius with those reported in Hansen *et al.* (1997) (open symbols). Results for water are denoted by circles, those for oil by squares. The grey lines are the prediction of the model developed by Rojas *et al.* (2010). The jump radius is identified with the position of the point of maximum curvature as shown in the insets (not to scale).

Most of the simulations below refer to the case of a jet Reynolds number $Re_j = 2aQ/(\pi a^2 \nu) \simeq 152.8$ with a the radius of the impinging jet. For a silicon oil with $\nu = 50 \times 10^{-6}$ m^{2}s^{-1} and a radius $a = 2.5$ mm, this value of Re_j would correspond to a flow rate $Q = 30 \times 10^{-6}$ m^3 s^{-1}. The jet is introduced with a uniform velocity profile at a height equal to $3a$. The length of the computational domain is $24a$, although in many figures only a portion of length $16a$, which is little influenced by the right boundary condition, is shown. The height of the vertical section at the right end of the domain is $2a$ and free outflow conditions are imposed at the exit of the domain. Unless otherwise specified, the Bond number is $Bo = \rho g a^2 / \sigma = 2.83$ with, e.g. $\rho = 970$ kg m^{-3} and $\sigma = 0.021$ N m^{-1}.

Watson (1964) pointed out that the film generated by a circular jet falling vertically on a horizontal plate reaches a minimum thickness h_m upstream of the jump. We compared Watson's estimates of this minimum thickness and of its location with the results of our Navier–Stokes simulations, finding a good agreement and, on this basis, we chose h_m

951 A20-14

and its corresponding radial position r_m as initial conditions for the integration of the first-order equation (5.1). According to Watson, r_m occurs at $r_m \simeq 1.426 r_{bl}$, where r_{bl} is the position at which the growing viscous boundary layer just reaches the free surface. For r_{bl} he provides the estimate $r_{bl}/a \simeq 0.3155(Q/\nu a)^{1/3}$, an estimate which is also in close agreement with that given in Wang & Khayat (2019). The corresponding value of h_m is given by Watson's equation (24) and is

$$\frac{h_m}{a} \simeq 2.308 \left(\frac{\nu a}{Q}\right)^{1/3}. \tag{6.1}$$

Since, near the jet impact point, the flow velocity is large, the effect of the inclination of the cone surface may be expected to be small, which justifies the use of these relations also for $\beta \neq 90°$.

In § 10 we show results for a pulsating jet for which $Q = Q(t)$. In this case we use (6.1) with the instantaneous value of Q. However, in order to avoid the re-meshing that would be made necessary by the use of a time-dependent value of r_m, we use the same relation as for the constant-Q case simply replacing Q by its time average Q_0. With the typical amplitude used for the perturbation of Q, less than 10 % of the mean, the position of r_m if we were to use $Q(t)$ for its estimate would vary by less than 3.5 % compared with the estimate based on Q_0, which is a negligible amount.

Details on the integration of the time-dependent version of the reduced-order model are provided in Appendix C.

7. Phase plane analysis

Figure 4 shows the result of Navier–Stokes simulations for increasing β starting from $90°$ (colour). In order to compare with the solutions of the first-order model, surface tension is not included in these simulations. As will be explained presently, the first-order model exhibits a critical point marked by an X in these figures. The solid lines are obtained by integrating (5.1) from upstream (purple) and downstream (red) of the jump using the Bogacki–Shampine method (Bogacki & Shampine 1989), a third-order Runge–Kutta method with the ability to automatically adapt the step size. The initial conditions for the former are as in (6.1). For the latter we start the backward integration at $r/a = 16$, i.e. upstream of the corner at the end of the inclined surface, in order to mitigate the influence of the boundary conditions at the right edge of the domain used for the Navier–Stokes simulations (see figure 15 for the shape of the solid boundary). For $\beta = 90°$ the initial film height at this position is taken from the NS result. For $\beta > 90°$, we use as starting value the large-r asymptotic solution of (5.1) given in (29) of Zollars & Krantz (1976) (which we have verified). Both lines closely follow the free surface as computed by the NS equations away from the jump region. As the jump is approached, they exhibit points of vertical tangency at which the integration is stopped. The distance between the two points of vertical tangency decreases with increasing inclination until the two lines smoothly join. Correspondingly, the film becomes smoother suggesting a gradual weakening of the jump.

The main point that emerges from the detailed explanation of these results which, by necessity, is somewhat intricate, is that the jump disappears as the surface of the cone becomes more inclined. The cone aperture at which this happens depends on the liquid properties as shown in figure 8.

We study the first-order equation (5.1) as a dynamical system in the phase plane (h, r) following Tani (1949), Bohr *et al.* (1993), Fernandez-Feria *et al.* (2019) and others. To
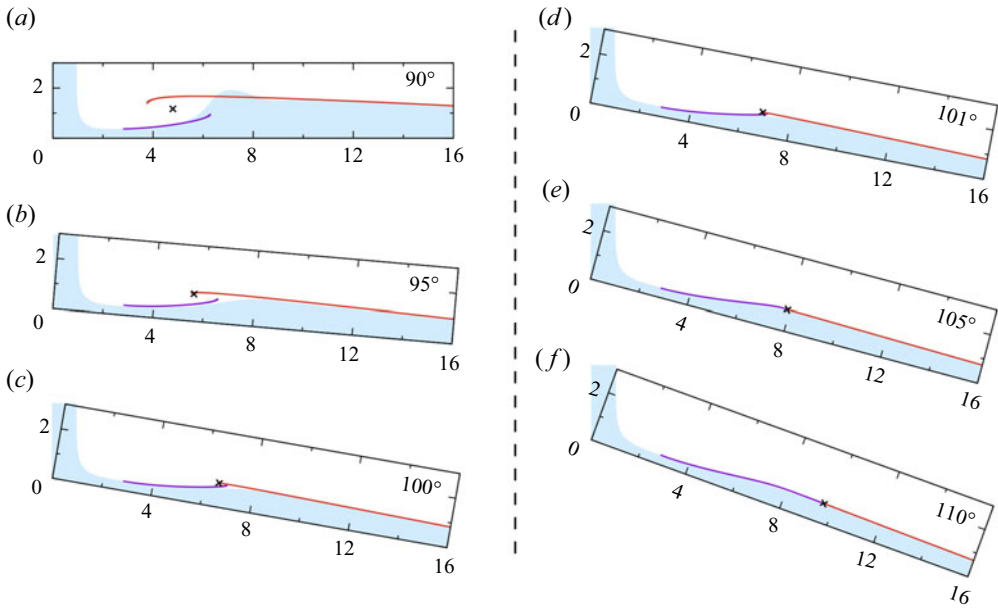
Figure 4. The colour shows the film profile as obtained from the Navier–Stokes simulations without surface tension for several cone inclinations β starting with a horizontal surface for $\beta = 90°$; the horizontal axis is r/a and the vertical axis h/a. The purple and red lines are obtained by integrating the first-order model (7.3) starting at the left and right of the critical point, respectively; the X marks the position of the critical point which, as explained in the text, should not be confused with the position of the jump. The parameter N defined in (7.4) has the value $N = 0.1046$ and the jet Reynolds number is $Re_j \simeq 152.8$.

simplify the presentation, it is expedient at this point to make use of dimensionless variables introducing the length scale

$$\ell = \left(\frac{54q^2}{35g}\right)^{1/5} \simeq 1.091 \left(\frac{q^2}{g}\right)^{1/5}. \tag{7.1}$$

The physical meaning of this quantity can be elucidated by noting that the velocity of a film falling by gravity over a distance ℓ would be $\sim \sqrt{g\ell}$. If the film cross-section is ℓ^2, the corresponding q would be $q \sim \ell^2 \sqrt{g\ell} = \sqrt{g\ell^5}$. Thus, ℓ is of the order of the length scale necessary to provide a freely falling film with the flow rate q under the stated conditions. We non-dimensionalize h and r by

$$\hat{h} = \frac{h}{\ell}, \quad \hat{r} = \frac{r}{\ell}. \tag{7.2a,b}$$

With this step, the first-order equation (5.1) for h becomes

$$\left(\frac{1}{\hat{r}^2 \sin^2 \beta} - \hat{h}^3 \sin \beta\right) \frac{d\hat{h}}{d\hat{r}} = \hat{h}^3 \cos \beta - \frac{\hat{h}}{\hat{r}^3 \sin^2 \beta} + \frac{N}{\hat{r} \sin \beta}\left(1 + \cot \beta \frac{\hat{h}}{\hat{r}}\right), \tag{7.3}$$

in which, besides β, an additional dimensionless viscosity parameter N appears given by (see also Kasimov 2008)

$$N = 3\left(\frac{35}{54}\right)^{4/5} \frac{\nu}{(q^3 g)^{1/5}} \simeq 2.121 \frac{\nu}{(q^3 g)^{1/5}}. \tag{7.4}$$

951 A20-16

With $q \sim \ell^2 \sqrt{g\ell}$ it is seen that $N \sim \nu/\sqrt{g\ell^3}$, which is of the order of the inverse of the Galilei number based on the length ℓ. It is easily shown that $\ell/a = \frac{9}{70}Re_j N \simeq 0.1286 Re_j N$.

Following a standard procedure, we rewrite (7.3) in parametric form in terms of a parameter s as

$$\frac{d\hat{h}}{ds} = \hat{h}^3 \cos \beta - \frac{\hat{h}}{\hat{r}^3 \sin^2 \beta} + \frac{N}{\hat{r} \sin \beta} \left(1 + \cot \beta \frac{\hat{h}}{\hat{r}}\right), \tag{7.5}$$

$$\frac{d\hat{r}}{ds} = \frac{1}{\hat{r}^2 \sin^2 \beta} - \hat{h}^3 \sin \beta. \tag{7.6}$$

The solutions of (7.3) have an extremum where $d\hat{h}/d\hat{r}$ vanishes, i.e. along the nullcline

$$F(\hat{h}, \hat{r}) \equiv \hat{h}^3 \cos \beta - \frac{\hat{h}}{\hat{r}^3 \sin^2 \beta} + \frac{N}{\hat{r} \sin \beta} \left(1 + \cot \beta \frac{\hat{h}}{\hat{r}}\right) = 0. \tag{7.7}$$

Along the other nullcline

$$G(\hat{h}, \hat{r}) \equiv \frac{1}{\hat{r}^2 \sin^2 \beta} - \hat{h}^3 \sin \beta = 0, \tag{7.8}$$

$d\hat{h}/d\hat{r}$ is infinite and the tangent to the solutions vertical.

The two nullclines cross at the critical point $(\hat{h}_c, \hat{r}_c)$ of the system, i.e. for

$$\hat{h}_c = \frac{1}{\sin \beta \hat{r}_c^{2/3}}, \tag{7.9}$$

with $\hat{r}_c$ given by $F(\hat{h}_c, \hat{r}_c) = 0$, i.e.

$$\left(1 + \frac{\cot \beta}{\hat{r}_c^{5/3} \sin \beta}\right) N + \frac{\cot \beta}{\hat{r}_c \sin \beta} - \frac{1}{\hat{r}_c^{8/3} \sin^2 \beta} = 0. \tag{7.10}$$

For $\beta = 90°$ this equation gives $\hat{r}_c = N^{-3/8}$ or

$$r_c = \ell N^{-3/8} = c_B \frac{q^{5/8}}{\nu^{3/8} g^{1/8}}, \tag{7.11}$$

with $c_B = 3^{-3/8}(\frac{54}{35})^{1/2} \simeq 0.823$. This is reminiscent of the scaling relation proposed in Bohr *et al.* (1993) which, for $\beta = 90°$, approximately identified the position of the jump with the critical point of their equation system. They suggest a smaller dimensionless coefficient, $c_B \simeq 0.73$, which is probably a consequence of the slightly different numerical coefficients in the equations. For general β, a simple graphical argument shows that (7.10) always has a positive solution. Figure 5 shows the dependence of the radial position of the critical point on the viscosity parameter N for several values of the angle β. The solid portion of the curves corresponds to the critical point being a spiral, while the dashed portion is for the critical point being a node. For $\cos \beta < 0$ and N small, we have $\hat{r}_c \simeq (-\cot \beta/\sin \beta)N^{-1}$ while, for N large, $\hat{r}_c \simeq (-\cot \beta/\sin \beta)^{3/5}$. For $\cos \beta > 0$ and small N, $\hat{r}_c \simeq (\cos \beta)^{-3/5}$ while, for large $N \cos \beta$, $\hat{r}_c \simeq (N \cos \beta)^{-1}$.
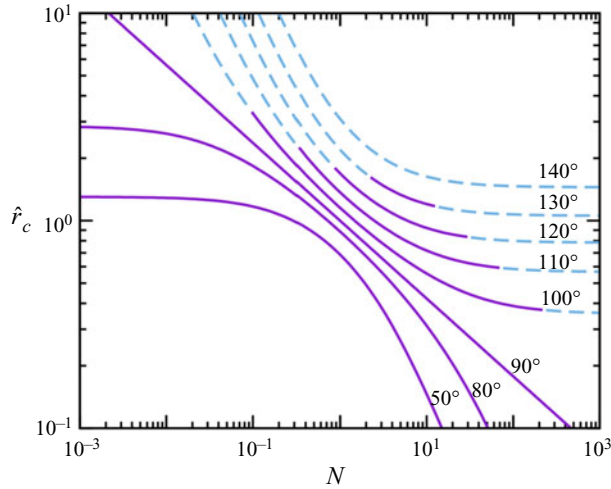
Figure 5. Dependence of the radial position of the critical point on the viscosity parameter N for several values of β. The solid portion of the curves corresponds to the critical point being a spiral, while the dashed portion is for the critical point being a node. As shown in figure 8 and as noted in the text, the critical point cannot be a spiral for β greater than approximately $134.3°$.

Equation (7.9) shows that $\hat{r}_c \hat{h}_c^{3/2} = \sin^{-3/2}\beta =$ constant for $\beta =$ constant. Returning to dimensional quantities this relation may be written as

$$\frac{q}{r_c h_c^{3/2} g^{1/2}} = \sqrt{\frac{35}{54}} \sin^{3/2}\beta \simeq 0.805 \sin^{3/2}\beta. \tag{7.12}$$

For $\beta = 90°$, Duchesne *et al.* (2014) form a Froude number similar to the quantity on the left-hand side of this equation except that h_c and r_c are evaluated at the maximum of the surface elevation, and they report the intriguing observation of an independence of this quantity from the liquid flow rate. Their numerical constant on the right-hand side, however, is 0.33 rather than 0.805. This difference may be due to the fact that, by their definition, both r_c and h_c are larger than the coordinates of the critical point. Even with this difference, (7.12) lends support to the 'constant Froude number' observation of Duchesne *et al.* (2014) and suggests an extension to $\beta > 90°$.

Examples of the dependence of $\hat{r}_c$ and $\hat{h}_c$ on β are shown in figure 6(*a*). The radial position of the critical point rapidly increases with β, signalling an increase of the hydraulic jump radius. The film height at the critical point correspondingly decreases, as indicated by (7.9). Examples of the nullclines for increasing values of β (in the direction of the arrows) are shown in figure 6(*b*). The inclination angle has a small effect on the lines $G = 0$, but a very strong one on the lines $F = 0$.

The characteristic directions at the critical point are the eigenvectors of the matrix

$$\begin{vmatrix} \partial_{\hat{h}} F & \partial_{\hat{r}} F \\ \partial_{\hat{h}} G & \partial_{\hat{r}} G \end{vmatrix} \begin{vmatrix} A \\ B \end{vmatrix} = \lambda \begin{vmatrix} A \\ B \end{vmatrix}. \tag{7.13}$$

The eigenvalues are given by

$$\lambda_{1,2} = \frac{1}{2} \left[\partial_{\hat{h}} F + \partial_{\hat{r}} G \pm \sqrt{(\partial_{\hat{h}} F - \partial_{\hat{r}} G)^2 + 4 \partial_{\hat{r}} F \partial_{\hat{h}} G} \right], \tag{7.14}$$
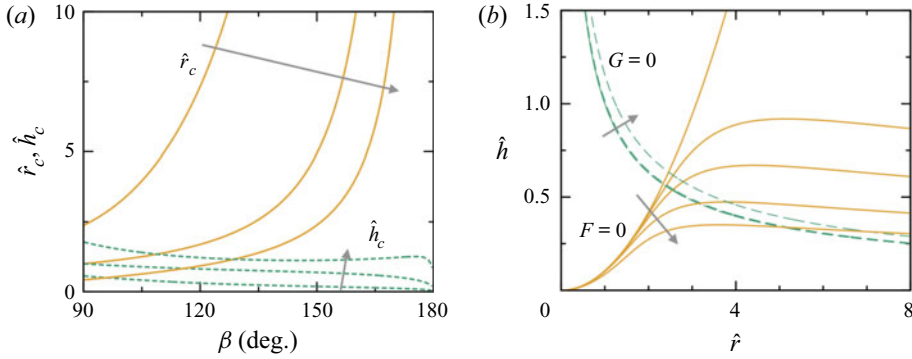
951 A20-18

Figure 6. (*a*) Dependence of the coordinates $\hat{h}_c$, $\hat{r}_c$ of the critical point on the angle β (defined in figure 1) for $N = 0.1$, 1 and 10, increasing in the direction of the arrows. (*b*) Examples of the nullclines $F = 0$ and $G = 0$. In the direction indicated by the arrows, the examples shown are for $\beta = 90°$, $91°$, $93°$, $100°$ and $120°$; here $N = 0.1046$. The nature of the critical point changes from spiral to node at $\beta_c = 100.52°$.

where all the partial derivatives are evaluated at the critical point $(\hat{h}_c, \hat{r}_c)$. The corresponding un-normalized eigenvectors have components

$$\left| 1, (\lambda_{1,2} - \partial_{\hat{h}} F)/\partial_{\hat{r}} F \right|^T, \tag{7.15}$$

or, equivalently, $|k, 1|^T$ with

$$k = \frac{\lambda_{1,2} - \partial_{\hat{r}} G}{\partial_{\hat{h}} G}, \tag{7.16}$$

the tangent of the angle between the eigenvectors and the r-axis. The radicand $\Delta = (\partial_{\hat{h}} F - \partial_{\hat{r}} G)^2 + 4\partial_{\hat{r}} F \partial_{\hat{h}} G$ in (7.14) is given by

$$\Delta = -\frac{23}{\hat{r}_c^6 \sin^4 \beta} + \frac{\cos \beta}{\hat{r}_c^2 \sin^2 \beta} \left[6 \left(N \cos \beta - \frac{1}{\hat{r}_c} \right) \hat{h}_c^2 + 9\hat{h}_c \cot \beta \right.$$
$$\left. + \frac{N}{\hat{r}_c^2 \sin^2 \beta} \left(N \cos \beta + \frac{14}{\hat{r}_c} \right) \right]. \tag{7.17}$$

For $\beta = 90°$ only the first term of (7.17), which is negative definite, gives a non-zero contribution. Thus, in this case, the eigenvalues are complex and the critical point is a spiral point to which the solution of the system (7.5), (7.6) tends asymptotically as the parameter s tends to infinity (see e.g. figure 2 in Bohr *et al.* (1993) and figure 1 in Fernandez-Feria *et al.* 2019). For any solution of (7.3) this implies the existence of points where $|dh/dr| \to \infty$, i.e. where the tangent to the spiralling trajectory becomes vertical as we have seen in figure 4. Of course, the solution loses physical meaning at the first such point to be encountered because, past it, trajectories coming from the left of the critical point (i.e. for increasing $\hat{r}$) would turn left and approach it in a retrograde manner, i.e. for decreasing $\hat{r}$, while trajectories coming from the right of the critical point (i.e. from decreasing $\hat{r}$) would approach it from the left, which would also be retrograde with respect to the original traversal direction of $\hat{r}$. As a consequence, a gap remains between the first two points of vertical tangency that cannot be bridged by the solution of the first-order system as it stands but, as will be seen in the next section, can be bridged by integration of the time-dependent version of the model with or without the surface-tension term
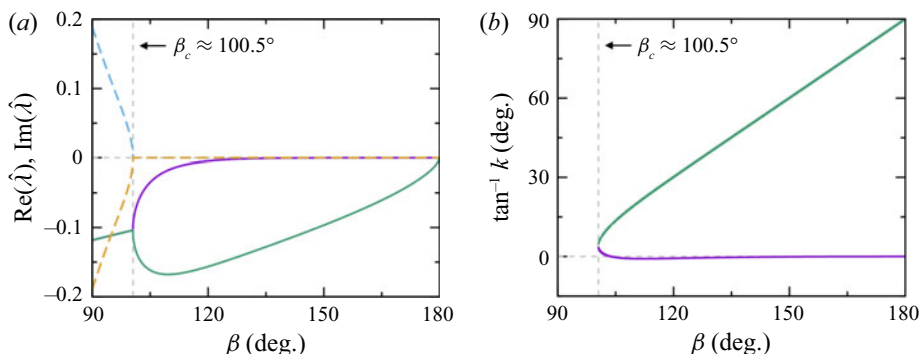
Figure 7. (*a*) Real (solid lines) and imaginary parts of the eigenvalues of the matrix in (7.13) at the critical point as functions of the angle β starting with a horizontal surface for $\beta = 90°$. The eigenvalues turn from complex to real at $\beta_c \simeq 100.5°$. (*b*) Angle between the eigenvectors of the matrix (7.13) and the *r*-axis; *k* is defined in (7.16). For this example $N = 0.1046$.

$(\sigma/\rho)\partial_r \mathcal{C}$. Rojas *et al.* (2010) attempted to bridge the gap including surface tension in their version of the time-independent model, but they were forced to postulate boundary conditions corresponding to a flat horizontal profile at the downstream boundary. In a later paper, Rojas, Argentina & Tirapegui (2013) determined the missing boundary conditions by minimizing the difference between their numerical results and the data of Bohr *et al.* (1996). In any event, it will be clear from the results of § 9 that, in steady-state conditions, surface tension only has the effect of selecting a smooth connection between the two branches of the solution of (7.3) thus providing what amounts to the internal structure of a 'quasi-shock' (Bohr *et al.* 1993) between the two points of vertical tangency. Several past authors have suggested that the position of the hydraulic jump may be close to the first point of vertical tangency of the left branch, both in two (see e.g. Singha *et al.* 2005) and three dimensions (see e.g. Tani 1949; Bohr *et al.* 1993; Wang & Khayat 2019), although, as the example of figure 4(*a*) shows, this prescription may not be very accurate.

The situation is different for a cone with $\beta > 90°$ as the second term of (7.17) gradually increases until a critical angle β_c is reached at which the radicand of (7.14) vanishes, becoming positive for $\beta > \beta_c$. At $\beta = \beta_c$ the critical point turns from a spiral into a node with equal real eigenvalues. As β increases beyond β_c, the eigenvalues remain purely real, the smaller one keeping close to zero (figure 7*a*). The angle that the two eigenvectors make with the *r*-axis is shown in figure 7(*b*). The angle corresponding to the smaller eigenvalue is slightly positive very near β_c, but turns negative and close to zero just a few degrees above. The angle of the larger eigenvalue instead rapidly increases. This major change of the nature of the critical point is mirrored by a major change of the nullclines $F = 0$ as shown in figure 6(*b*). While for $\beta = 90°$ the nullcline $F = 0$ is proportional to $\hat{r}^2$, as β increases, it develops a maximum and bends downward tending to 0 at infinity. With increasing β the maximum decreases and the slope of the eigenvectors at the critical point becomes negative (figure 7*b*).

A graph of β_c vs N is shown in figure 8. The dashed lines approximate the curve for small and large values of N; they are approximated very well by the numerical fits

$$\beta_c \simeq \frac{\pi}{2} + 0.75\,N^{0.62} \quad \text{and} \quad \beta_c \simeq \frac{\pi}{2} + 5.2\,N^{-0.62}, \qquad (7.18a,b)$$

respectively. The critical angle is close to 90° for small viscosity, rises to a maximum of approximately 134.3° at $N \simeq 5.5$ and then re-descends toward 90°. The rising branch
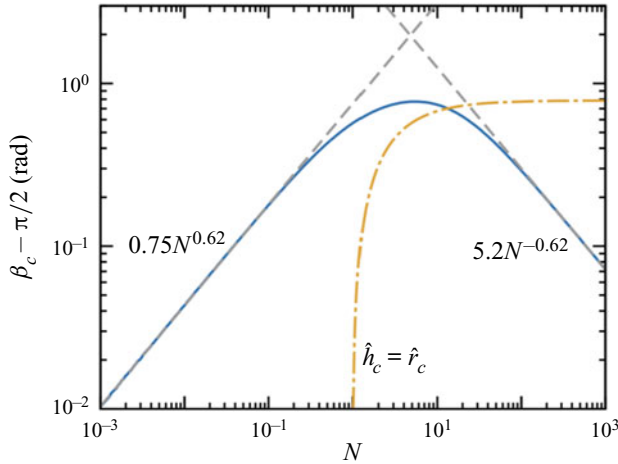
951 A20-20

Figure 8. Dependence of the critical angle β_c on the viscosity parameter N defined in (7.4). The dashed lines show the approximations (7.18a,b) for small and large N. When $\beta = \beta_c$, the critical point of the system (7.5), (7.6) changes from spiral to node. The dash-dotted line represents the locus $\hat{r}_c = \hat{h}_c$ given by (7.19) which limits the quantitative validity of the present model. (Note that, for this line, the ordinate axis is actually $\beta - \pi/2$ rather than $\beta_c - \pi/2$).

corresponds to the fact that, with increasing viscosity, the inclination necessary to replenish the momentum lost to viscous effects increases. Interpretation of the descending portion of the curve for larger N requires some care because, as is evident from figure 6(a), for large N, $\hat{r}_c$ can be smaller than $\hat{h}_c$ thus violating the basic separation-of-scales assumption on which the mathematical model is built. It is easy to show that $\hat{r}_c = \hat{h}_c$ along the line

$$N = -\frac{\cot\left(\beta + \dfrac{\pi}{4}\right)}{\sin^{2/5}\beta}, \tag{7.19}$$

a relation represented by the dash-dotted line in figure 8; to the right of this line $\hat{r}_c < \hat{h}_c$. Although the present model's predictions cannot be trusted quantitatively in this parameter range, it is reasonable to expect that, when viscosity is large, the momentum loss is very rapid and a modest inclination is sufficient to maintain the Nusselt-like flow (5.3).

The change of the nature of the critical point from spiral to node 'nearly' eliminates the discontinuous solutions found for $\beta = 90°$ in the sense that all relevant solutions of the system (7.5), (7.6) become continuous just a few degrees above β_c. The explanation of this fact requires the consideration of some details and will be found in Appendix A. Here, we illustrate the point with figure 9 in which the solid lines are the nullclines and the short dashed lines the eigenvectors at the critical point. The purple lines are the solutions of the steady model approaching the node along the eigenvector corresponding to the 'fast' (larger) eigenvalue (which has the greater inclination). In the figure, shading indicates the regions which contain initial conditions for the integration of (7.5), (7.6) such that the solution is guaranteed to approach the critical point from the left without a retrograde portion (recall from the theory of dynamical systems (see e.g. Lefschetz 1963; Glendinning 1994; Strogatz 2015) that solutions approach the critical point along the direction (eigenvector) corresponding to the smaller eigenvalue). On the right these regions are bounded by the purple lines, i.e. the solutions that reach the critical point
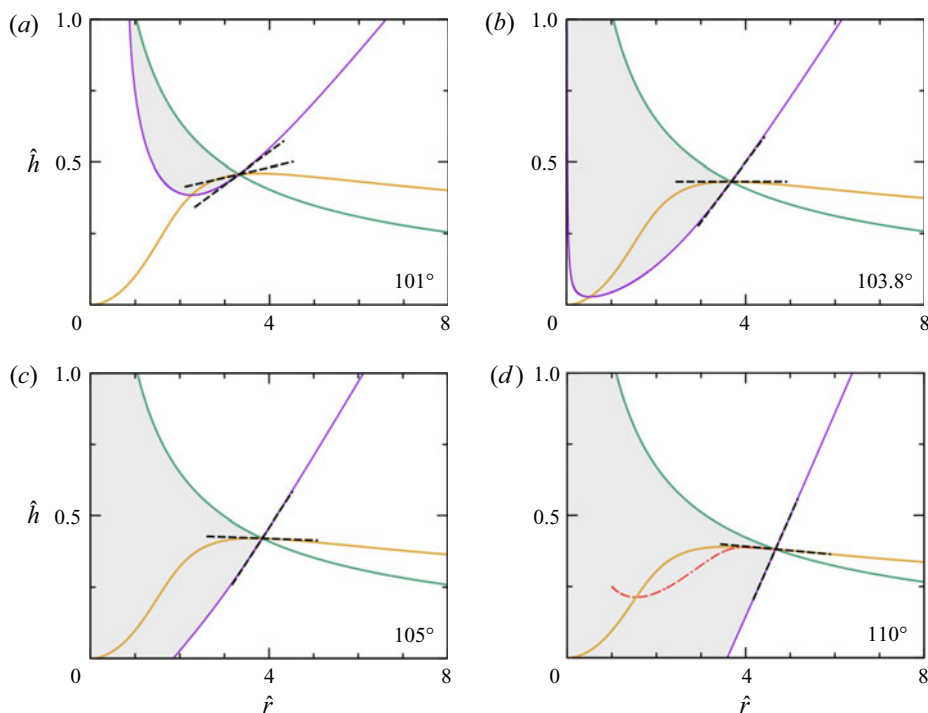
Figure 9. The figures show the nullclines $F = 0$ (yellow) and $G = 0$ (green) in the phase plane of the system for $N = 0.1046$ and (a) $\beta = 101°$, (b) $\beta = 103.8°$, (c) $\beta = 105°$ and (d) $\beta = 110°$; the critical angle is $\beta_c = 100.52°$. The short dashed lines crossing at the critical point are the eigenvectors (7.15) of the linearized system. Solutions starting at points in the shaded regions will approach the critical point from the left without a retrograde section similarly to the solution indicated by a dash-dotted line (red) in panel (d). The purple lines are the solutions of the steady model approaching the node along the eigenvector corresponding to the larger eigenvalue (with the greater slope). These lines are part of the boundaries of the shaded region because any solution starting to the right (or under) them must necessarily approach the critical point from the right.

along the 'fast' eigenvalue, because any solution starting from the right of this line will necessarily approach the critical point from the right. For $\beta = \beta_c$ the critical point is a star and all solutions ultimately tend to it along straight lines. The region without retrograde approach is small for β close to β_c (figure 9a), but it expands very rapidly as β is increased just a few degrees until, for $\beta = 105°$, it has basically invaded the entire area to the left of the nullcline $G = 0$ where physically relevant initial conditions can be situated.

Although the figure also shows regions with an initial value of $\hat{h}$ greater than $\hat{h}_c$, for the situations of present concern we would be more interested in initial conditions such that the film thickness approaches $\hat{h}_c$ from below as, for example, the solution indicated by the dash-dotted line in figure 9(d). A similar shading could be used to the right of the critical point to identify initial conditions such that the backward-integrated solution (i.e. for decreasing $\hat{r}$) would approach the critical point without a retrograde section, but this region coincides with the area between the two nullclines to the right of the critical point except for a small portion which completely disappears as soon as the slope of the eigenvector becomes negative which, in this example, happens at $\beta \simeq 103.8°$ (see Appendix A).

The fact that at $\beta = \beta_c$ the nature of the critical point changes from spiral to node, and that just a few degrees above this point effectively the relevant solutions do not have a

951 A20-22

retrograde section, suggests that $\beta = \beta_c$ can plausibly be adopted as the condition for the disappearance of the hydraulic jump.

8. The time-dependent reduced-order problem

Including surface tension in the steady reduced-order model leads to a two-point boundary value problem which has proven numerically delicate in earlier investigations (see e.g. Watanabe *et al.* 2003). We have found that a more robust way to solve the steady problem is to consider the long-time asymptote of the time-dependent problem which, of course, is also of interest in itself.

The equations to be solved are (4.9) and (4.10) which we rewrite as the following system:

$$\partial_t \boldsymbol{H} + \boldsymbol{A}\partial_r \boldsymbol{H} = \begin{vmatrix} -\dfrac{\cot \beta\, h}{r^2 \sin \beta}\partial_r q \\ S \end{vmatrix}, \tag{8.1}$$

where the matrix $\boldsymbol{A}$ and the vector $\boldsymbol{H}$ are given by

$$\boldsymbol{A} = \begin{vmatrix} 0 & \dfrac{1}{r \sin \beta} \\ -\dfrac{9}{7}\dfrac{q^2}{rh^2 \sin \beta} + \dfrac{5}{6}rgh\sin^2 \beta & \dfrac{17}{7}\dfrac{q}{rh \sin \beta} \end{vmatrix}, \quad \boldsymbol{H} = \begin{vmatrix} h \\ q \end{vmatrix}, \tag{8.2a,b}$$

and the source term S by

$$S = -\frac{5}{6}hr \sin \beta \left(g \cos \beta - \frac{\sigma}{\rho}\partial_r \mathcal{C} \right) + \frac{9}{7}\frac{q^2}{hr^2 \sin \beta} - \frac{5}{2}\frac{vq}{h^2}\left(1 + \cot \beta \frac{h}{r} \right). \tag{8.3}$$

Note that the surface-tension term has been grouped with the other source terms in spite of its differential nature as, otherwise, conversion of the model to a first-order system would cause difficulties. The importance of this term away from the critical point is minor. We have also placed a small term proportional to $\partial_r q$ on the right-hand side of the first equation to simplify the developments that follow.

The description of a numerical method for the solution of (8.1) can be found in Appendix C. Here, we focus on the mathematical nature of the problem starting with an investigation of the eigenvalues of the matrix $\boldsymbol{A}$ which are given by

$$\lambda_{\pm} = \frac{17q}{14rh \sin \beta} \pm \frac{1}{2}\sqrt{\frac{37q^2}{49r^2\, h^2 \sin^2 \beta} + \frac{10}{3}gh \sin \beta}. \tag{8.4}$$

Since the radicand is positive–definite, the system is unconditionally hyperbolic. One eigenvalue, λ_+, is always positive. The other one, λ_-, changes sign from positive to negative precisely when the term in parentheses multiplying $\mathrm{d}h/\mathrm{d}r$ in (5.1) turns from positive to negative with increasing h or r. When both eigenvalues are positive, i.e. when h is small upstream of the jump, information propagates only in the direction of increasing r and the flow may then be said to be super-critical as there is no back-propagation effect. Conversely, when h has become so large that λ_- has changed sign, i.e. here, downstream of the jump, the flow is subcritical.

The Riemann invariants are the elements of the vector $\boldsymbol{R}^{-1}\boldsymbol{H}$ in which the matrix $\boldsymbol{R}$ is such that $\boldsymbol{R}^{-1}\boldsymbol{AR}$ is diagonal; $\boldsymbol{R}$ is constructed with the eigenvectors of $\boldsymbol{A}$ and it is

951 A20-23

proportional to

$$\boldsymbol{R} = \begin{vmatrix} (r \sin \beta)^{-1} & (r \sin \beta)^{-1} \\ \lambda_+ & \lambda_- \end{vmatrix}.$$ (8.5)

The Riemann invariants are found to be given by

$$C_\pm = \frac{r \sin \beta}{\lambda_+ - \lambda_-} \left(\pm \lambda_\pm h \mp \frac{q}{r \sin \beta} \right).$$ (8.6)

We can use (8.1) integrated to steady state to generate results for the jump radius omitting surface-tension effects; the numerical method used for this purpose is described in Appendix C. The critical aspect of the method that explains its ability to avoid dealing with the singularity of the time-independent model is the coupling that it introduces between the flow upstream and downstream of the critical point. The same coupling also implies the continuity of mass and momentum fluxes and, therefore, automatically includes the conservation relations that, starting with Watson (1964), many previous authors have used to determine the location of the hydraulic jump.

As already noted more than once, including the horizontal plate case $\beta = 90°$ would force us to use a boundary condition at the right edge of the computational domain for which many choices are possible which lead to different results. On the other hand, with a sloping cone, the large-r asymptotic solution of (5.1) given by Zollars & Krantz (1980) gives a unique well-defined prescription which permits us to obtain results with a certain degree of universality; we impose this condition at $\hat{r} = 12$. We consider cone angles between $95°$, which is a sufficient slope for the application of the downstream boundary condition, and $110°$, with the upper limit dictated by the decreasing N-range for the existence of the jump as shown in figure 5. At the left boundary of the domain we choose as initial condition $\hat{h} = 0.1$ at $\hat{r} = 0.2$. We have found some slight dependence of the jump radius on this choice, especially when the jump radius is small, but not strong enough to significantly affect the scaling shown in figure 10, namely

$$\hat{r}_{jump} \simeq 1.2 \left[1 + \frac{\beta - 90°}{60°} \right] N^{-0.41},$$ (8.7)

with β in degrees. In terms of dimensional quantities, this relation becomes

$$r_{jump} \simeq 0.962 \left[1 + \frac{\beta - 90°}{60°} \right] \frac{q^{0.646}}{\nu^{0.41} g^{0.118}}.$$ (8.8)

The scaling proposed by Bohr *et al.* (1993) for a horizontal plate is $0.73 q^{0.625} \nu^{-0.375} g^{-0.125}$ and is comparable to (8.8) for $\beta = 90°$.

9. The effect of surface tension

We can now show the effect of surface tension on the flows presented at the beginning of § 7. As mentioned before, we have found expedient to run the time-dependent model to steady state to generate these results, some of which are shown in figures 11 and 12. We begin by comparing in the former figure the results of the reduced-order model with and without surface tension for $\beta = 90°$, $95°$ and $105°$. The critical angle for this case is $\beta_c = 100.52°$, so that the first two cases have a smaller slope and exhibit a hydraulic jump while in the last one the solution is very smooth and the jump virtually gone. As shown by the symbols in figure 11, the numerical method for the time-dependent model described in the previous section is able to sharply capture the discontinuity of the solution without
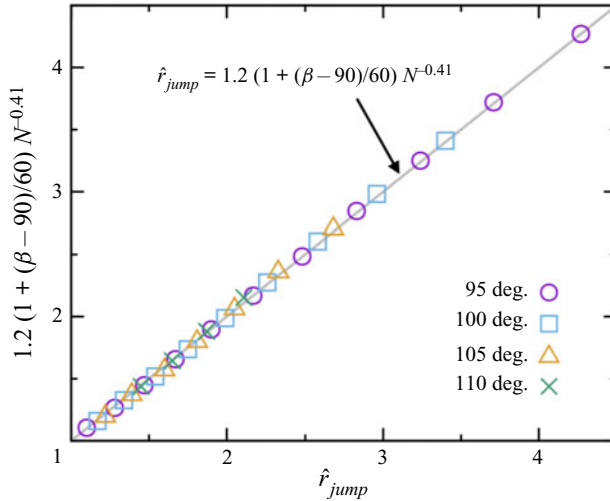
951 A20-24

Figure 10. Scaling of the hydraulic jump radius as predicted by the long-time (steady) solutions of the time-dependent, reduced-order model (8.1) without surface tension.
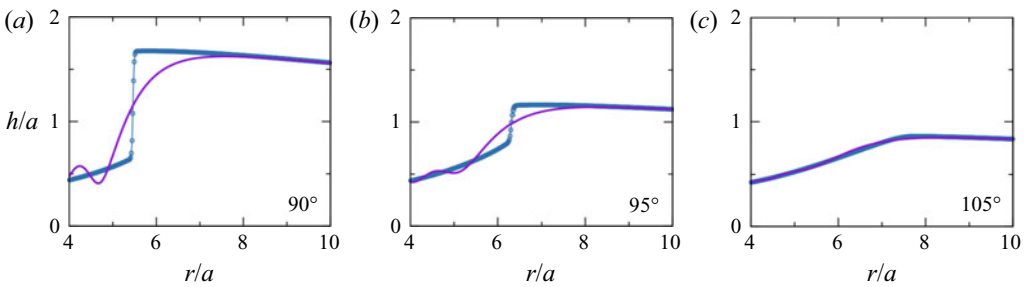

Figure 11. Steady solutions of the time-dependent two-equation system (8.1) with (continuous lines) and without surface tension. Here, $N = 0.1046$ with a corresponding critical angle $\beta_c = 100.52°$.

surface tension. With the inclusion of surface tension, the solution exhibits oscillations upstream of the jump, which are a known artefact of first-order models (see e.g. figure 5 in Ruyer-Quil & Manneville 2000), and are also visible e.g. in figure 2 of Rojas *et al.* (2013).

Figure 12 compares some of the solutions of the steady first-order model already shown in figure 4 (dashed lines in the left column) with the long-time (steady) solutions of the time-dependent version of the model (solid lines); the X marks the position of the critical point which, in both cases, is seen to be to the left of the discontinuity. Away from the critical point the steady and time-dependent solutions agree very well. The right column compares the Navier–Stokes simulations with the results of the time-dependent reduced-order model including surface tension (solid lines). Other than for the small oscillations upstream of the jump already mentioned, the reduced-order model with surface tension does a good job at reproducing the NS results. Both in these cases and in those of the previous figure the Bond number is $Bo = \rho g a^2 / \sigma \simeq 2.83$.

The results of the Navier–Stokes simulations for the free-surface profiles corresponding to some of the water data points in figure 3 are shown by the thin grey line in figure 13 where they are compared with the present time-dependent reduced-order model; the boundary conditions for the latter are obtained from the Navier–Stokes simulations.
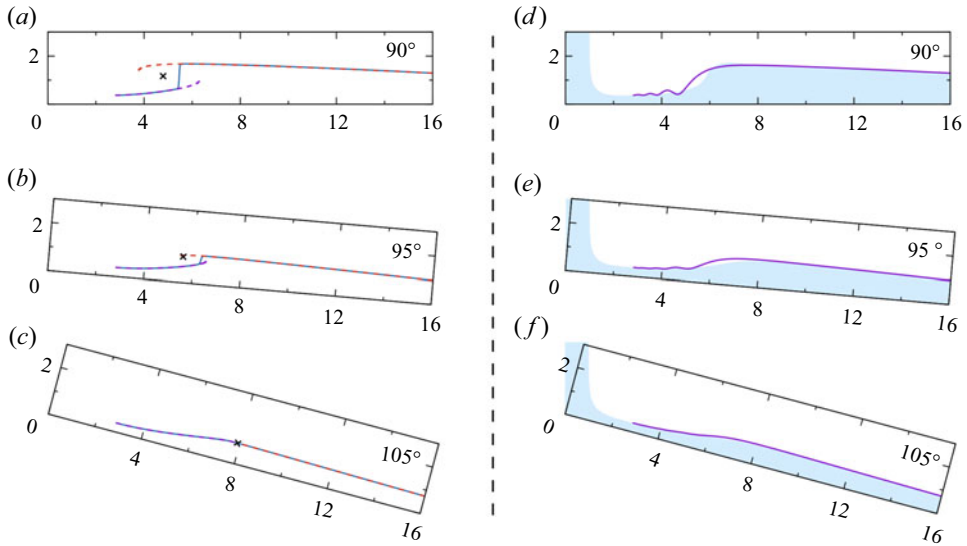
Figure 12. The images in the left column are for cases (*a*), (*b*) and (*e*) of figure 4 and show the solution of the reduced-order model; the horizontal axis is r/a and the vertical axis h/a. The dashed lines have been obtained by integrating the time-independent model (5.1) starting from the left and the right of the critical point, the position of which is marked by the X. The long-time (steady) solutions of the system (8.1) without surface tension, obtained by the numerical method described in § 8, are shown by the solid lines. The images in the right column compare the solution of the reduced-order model with surface tension (solid line) with the NS results including surface tension. The viscosity parameter N defined in (7.4) has the value $N = 0.1046$, the critical angle is $\beta_c = 100.52°$, the Bond number $Bo = 2.832$ and the jet Reynolds number is $Re_j \simeq 152.8$.

The yellow solid lines and the purple dashed lines are the model results with and without surface tension effects, respectively. It is evident that surface tension smoothens the free surface in the jump region but has virtually no effect on the jump position. Figure 14 compares the same data of Duchesne *et al.* (2014) already shown in figure 2 (crosses) with those obtained by the present numerical method with and without surface tension; the former are shown by the slightly smoother solid curve (orange). Comparison of the two reduced-order model results confirms that surface tension only has a minor effect.

This conclusion is further supported by the NS results for different values of the Bond number shown in figure 15. In descending order, the images are for $Bo = \infty$ (zero surface tension), 5.66, 2.83 and 1.42. For small or no surface tension the film profile exhibits a hump right downstream of the jump, which is also present in the results of Wang & Khayat (2021) (see the second panel of their figure 7). Increasing surface tension prevents the formation of this feature but has otherwise very minor effects.

10. Pulsating jet

We have shown a few examples of results obtained as the long-time limit of the time-dependent formulation. We now compare the two-equation time-dependent model with the Navier–Stokes simulations for a case in which the flow rate of the jet oscillates sinusoidally with frequency f

$$Q(t) = Q_0 + Q_1 \sin(2\pi ft). \tag{10.1}$$

Two examples, taken after steady conditions have been reached, are shown in figures 16 and 17 where the vertical scale is magnified by a factor of 10 with respect to the horizontal
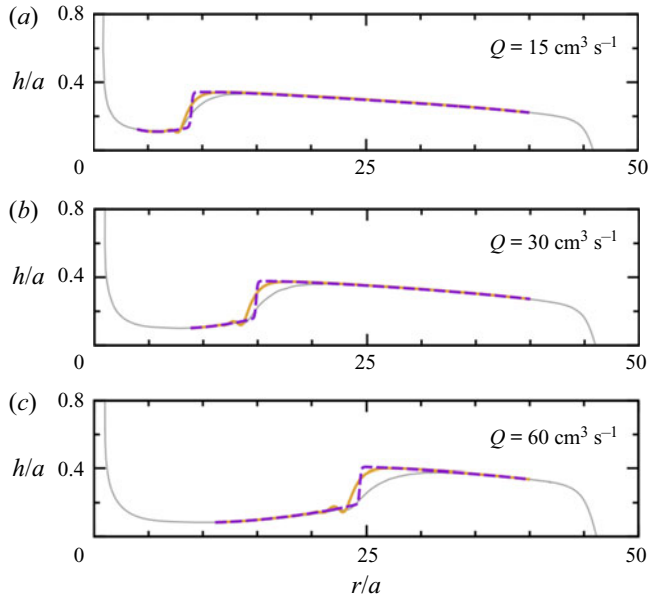
951 A20-26

Hydraulic jump on a cone

Figure 13. The thin grey lines are the present NS results for three cases for which the jump radius was shown in figure 3. The yellow solid lines and the purple dashed lines are the steady-state results given by the time-dependent model with and without surface tension terms, respectively.
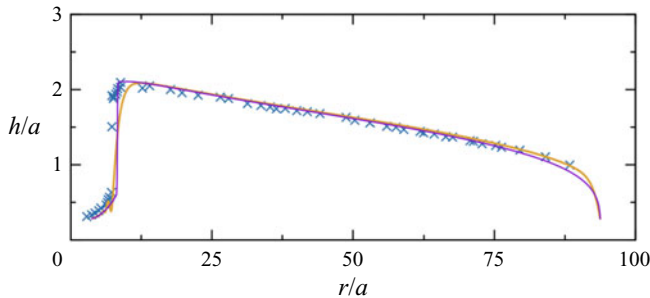

Figure 14. The data of Duchesne *et al.* (2014) shown in figure 2 (crosses) compared with the time-dependent reduced-order model predictions with (orange line) and without (purple line) surface tension.

one. In both cases $Q_1/Q_0 = 0.05$, $\beta = 120°$, $Re_{j0} = 2Q_0/(\pi a \nu) = 382$ and $N = 0.0419$. For figure 16 $a^2 f/\nu = 2.5$ while, for figure 17, the frequency is twice as large, $a^2 f/\nu = 5.0$ (these values are realizable with all the same parameter values as before except for the kinematic viscosity $\nu = 20 \times 10^{-6}$ m^2 s^{-1} and frequencies of 8 and 16 Hz). A longer sequence showing the reduced-order model simulation for the first case over an extended domain is available as Movie 1 of the supplementary material associated with this paper. The movie shows how the waves gradually get shorter as they are damped by the combined effect of geometry and viscosity.

The two panels in each figure are separated by half a period, the first image corresponding to the phase $2\pi ft = 0.233 \times (2\pi)$ and the second one to $0.733 \times (2\pi) = 0.233 \times (2\pi) + \pi$. The colour shows the NS results and the solid line the results of the time-dependent two-equation model. Since this latter model does not include the jet, it
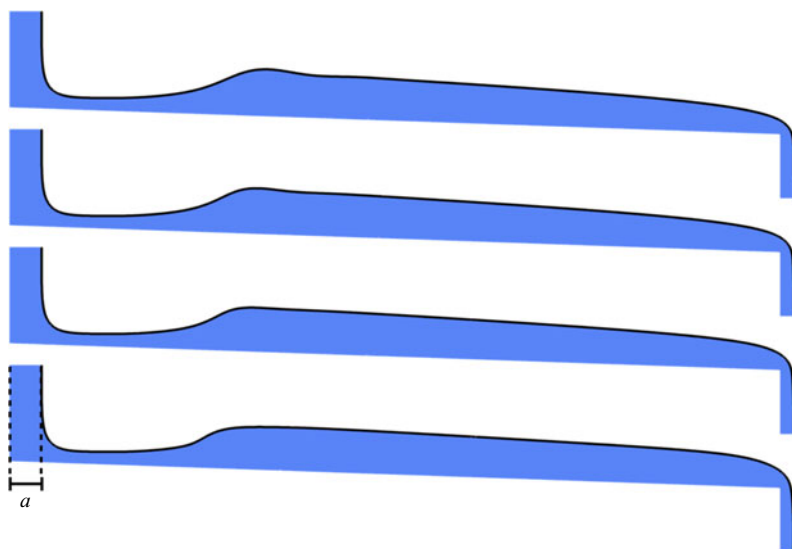
951 A20-27

Figure 15. Effect of surface tension on the film profile as obtained from the Navier–Stokes simulations with $\beta = 92°$, $N = 0.1046$. From top to bottom the Bond number has values ∞ (no surface tension), 5.66, 2.83 and 1.42. The jet Reynolds number is $Re_j = 152.8$.
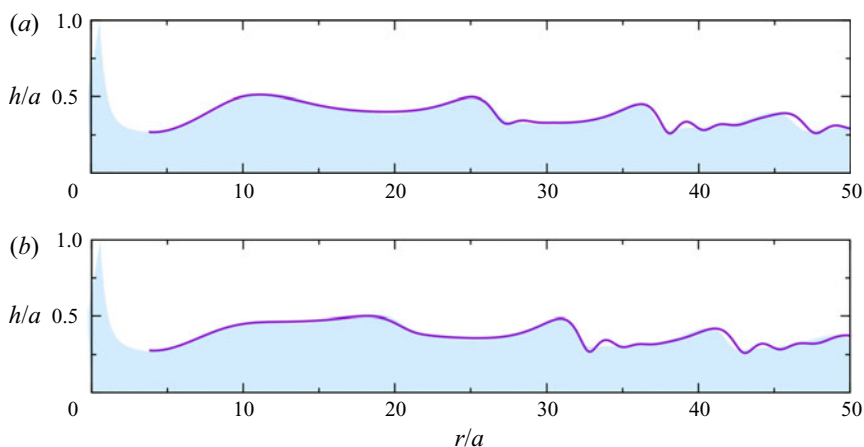

Figure 16. Two frames from the direct numerical simulation of a sinusoidally pulsating jet (10.1) with an average Reynolds number $Re_{j0} = 382$, a normalized frequency $a^2 f / \nu = 2.5$ and $N = 0.0419$. The purple lines are results of the time-dependent reduced-order model of § 8. The two images are separated by one half-period.

cannot be synchronized *a priori* with the Navier–Stokes simulation. The result shown in the figure is obtained by translating in time the results of the reduced-order model in such a way that the phase of the first several waves matches that of the NS results.

Close to the point of impingement of the jet the film thickness gradually increases but, since the inclination angle is much greater than the critical angle $\beta_c = 96.0°$, conditions are far from those producing a jump. Immediately downstream the film is relatively thick but very quickly the free surface settles into a series of steady waves preceded by capillary oscillations and followed by a long tail reminiscent of the Kapitza waves on a two-dimensional film. The reduced-order model does a good job for the lower-frequency
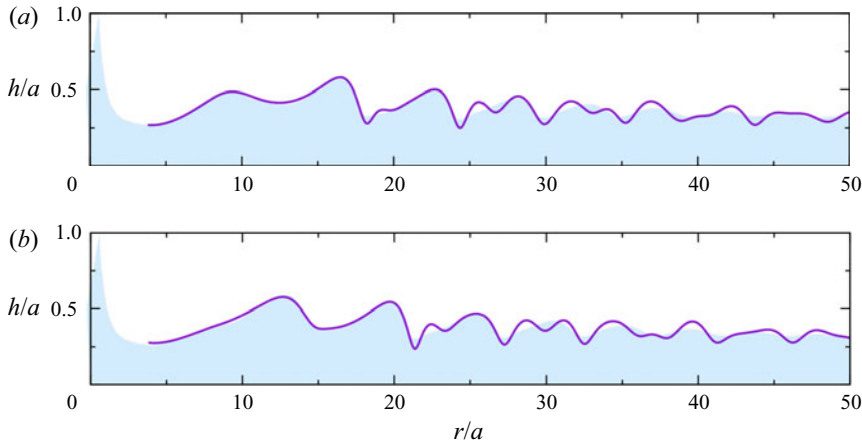
951 A20-28

Figure 17. Two frames from the direct numerical simulation of a sinusoidally pulsating jet (10.1) with an average Reynolds number $Re_{j0} = 382$, and a frequency twice as large as in the previous figure, $a^2 f / \nu = 5.0$; $N = 0.0419$. The purple lines are results of the time-dependent reduced-order model of § 8. The two images are separated by one half-period.

case of figure 16, but is not as accurate for the larger-frequency example of figure 17. Particularly in the higher-frequency case of figure 17, some of the short waves exhibited by the reduced-order model have a slightly larger amplitude than the NS ones, which is another manifestation of a tendency that we have already encountered in figure 12. Overall, however, the agreement is quite satisfactory.

The supplementary material associated with this paper includes a few other examples of situations for which, in steady conditions, the jet would produce a jump. These sequences show that, as the flow rate increases, a jump builds up. This is followed by a wave which originates on the downstream side of the jump and propagates outward. As the flow rate decreases the jump smoothes out, then builds up again generating another wave and so on. In no case we observe waves propagating upstream in the thin part of the film, confirming the super-critical nature of the flow in this region.

11. Reverse gravity

The reduced-order model (4.9), (4.10) can be adapted to the case of a jet striking the cone from below by reversing the direction of the polar axis, which has the effect of changing the sign of g. A cone with a downward aperture then has $0 < \beta < \pi/2$ while, if the aperture is upward, $\pi/2 < \beta < \pi$. The continuity equation (4.9) remains unchanged, while the other equation becomes

$$
\partial_t q + \frac{17}{7} \frac{q}{hr \sin \beta} \partial_r q - \frac{5}{6} \left(\frac{54}{35} \frac{q^2}{h^2 r \sin \beta} + grh \sin^2 \beta \right) \partial_r h
$$
$$
= \frac{5}{6} rh \sin \beta \left(g \cos \beta + \frac{\sigma}{\rho} \partial_r \mathcal{C} \right) + \frac{9}{7} \frac{q^2}{hr^2 \sin \beta} - \frac{5}{2} \frac{\nu q}{h^2} \left(1 + \cot \beta \frac{h}{r} \right). \quad (11.1)
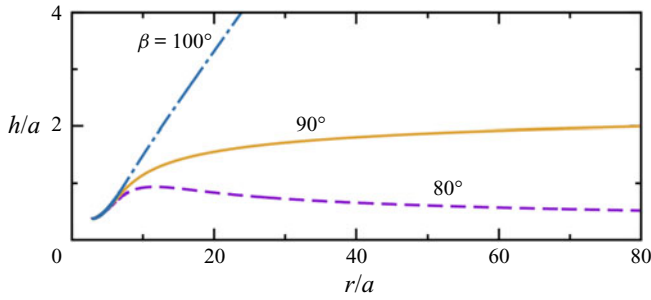$$

951 A20-29

Figure 18. Predictions of the steady first-order model (11.2), without surface tension, for the flow on the underside of the surface of a cone with three different apertures, upward, $\beta = 100°$, horizontal, $\beta = 90°$, and downward, $\beta = 80°$.

In particular, in steady conditions and omitting surface tension, we find, in place of (5.1),

$$\left(gh^3 \sin \beta + \frac{54}{35} \frac{q^2}{r^2 \sin^2 \beta} \right) \frac{\mathrm{d}h}{\mathrm{d}r}$$

$$= -\frac{54}{35} \frac{hq^2}{r^3 \sin^2 \beta} - h^3 \, g \cos \beta + \frac{3\nu q}{r \sin \beta} \left(1 + \cot \beta \frac{h}{r} \right). \tag{11.2}$$

Provided $\cos \beta < 0$, so that the aperture of the cone is upward, for large r this equation becomes $\mathrm{d}h/\mathrm{d}r \simeq -\cot \beta$ so that h increases without bound; an example is the curve labelled $\beta = 100°$ in figure 18. This result is not surprising as, by using the steady version of the model, we have prevented the development of instabilities (in particular the Rayleigh–Taylor instability) and, since liquid has been injected at a constant rate for all times since $t \to -\infty$ and the velocity decreases with r, the predicted thickness of the film must diverge. If $\cos \beta > 0$, on the other hand, gravity assists the drainage of the film and one finds

$$h \simeq \left(\frac{3\nu q}{gr \sin \beta \cos \beta} \right)^{1/3}, \tag{11.3}$$

which coincides with (5.3) upon a change of the sign of g. An example is the curve labelled $\beta = 80°$ in figure 18; for $\beta = 90°$, $h \to (4N \log r)^{1/4}$.

Figures 19(a) and 19(b) show numerical results obtained from the time-dependent two-equation model including surface tension. In this case the Rayleigh–Taylor instability is not suppressed and, indeed figures 19(a) and 19(b) show it in action. Here, the time integration stops when the film has thinned so much as to require an unreasonably small time step (cf. Yiantsios & Higgins (1989, for a similar situation in two dimensions)). Figure 19(a) is for $Bo \simeq 2.43$ with $\beta = 90°$ and $100°$, while figure 19(b) is for $\beta = 90°$ with $Bo = 9.72$ and $Bo = 0.608$. The waves arise spontaneously due to the Rayleigh–Taylor instability and have a wavelength quite close to that of the fastest growing linear mode predicted by the theory of this instability for the present axisymmetric geometry.

For all the examples of figures 18 and 19 the flow rate is as specified in § 6 and corresponds to a jet Reynolds number $Re_j \simeq 152.8$. For figure 19 zero-gradient boundary conditions were imposed at the right end of the domain. The conditions at the left boundary of the domain were set using Watson's theory as described in § 6; in particular, integration started at $r_m/a \simeq 2.804$ with $h_m/a \simeq 0.3714$; a constant flow rate was maintained at
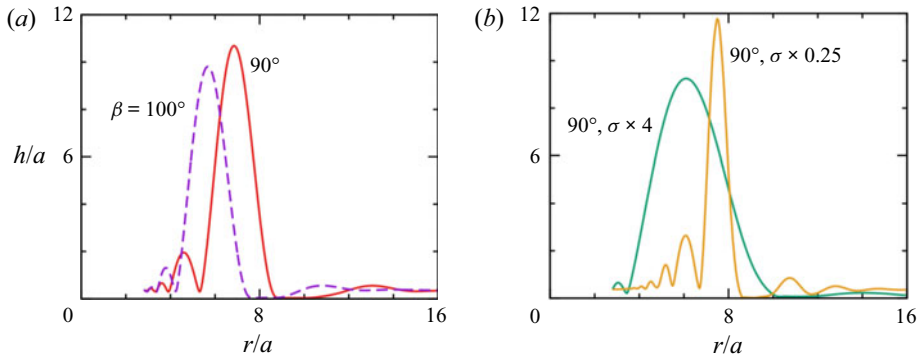
951 A20-30

Figure 19. Predictions of the time-dependent two-equation model (8.1), including surface tension. Panel (*a*) is for $Bo \simeq 2.43$ with $\beta = 90°$ and $100°$. Panel (*b*) is for $\beta = 90°$ with $Bo = 9.72$ and $Bo = 0.608$. In both cases the images shown are at the time when the film has become too thin for the integration to proceed.

$r_m/a \simeq 2.804$ and, initially, the cone surface was covered by a uniform liquid layer with $h_m/a \simeq 0.3714$.

It is known from the two-dimensional analogue of this configuration that a sufficient downward tilt of the plate can hinder the development of the Rayleigh–Taylor instability: as they propagate downward, surface waves grow under the combined effect of the Kapitza and Rayleigh–Taylor instabilities but, in suitable conditions, they can stabilize at a finite amplitude (see e.g. Indeikina, Veretennikov & Chang 1997; Brun *et al.* 2015; Kofman *et al.* 2018; Zhou & Prosperetti 2022). The same phenomenon is observed for three-dimensional drops sliding down the underside of an inclined surface (Jambon-Puillet *et al.* 2021). Without an imposed disturbance, in the present system the instability will grow only due to numerical errors and, for this reason, grid refinement does not lead to convergence of the results. We have found a variety of behaviours, with waves initially growing and then being damped, or approaching what seems to be a steady state, or slowly growing. Extending the computational domain increases the influence of numerical errors and we are therefore unable to describe the asymptotic behaviour of the system. One factor to keep in mind is that the mean velocity of the flow, which is proportional to h^2, decreases proportionally to $r^{-2/3}$ and, therefore, it may become too small to stabilize the waves.

Figure 20 shows the results of the Navier–Stokes simulations for a jet, again with $Re_j \simeq$ 152.8, impinging on a conical surface from below for inclinations $\beta = 80°$, $90°$ and $100°$. The contact angle with the solid surface is $90°$. The results have been obtained prescribing the total pressure at the lower boundary where the falling liquid leaves the computational domain. The difference from the results of the previous figure is due to the fact that, here, initially, the plate is dry while, in the previous case, at $t = 0$ it was covered by a uniform liquid layer. As the inclination angle of the cone surface is increased, the film detaches from the plate closer and closer to the axis of symmetry. None of these cases exhibits a structure resembling a hydraulic jump, with the film starting thin and then undergoing a rapid thickening. The results are qualitatively similar to those reported in the literature for so-called water bells (see e.g. Clanet 2007; Jameson *et al.* 2010). For this case, Button *et al.* (2010) gave the relation $r_d = c_d[\rho Q^3/(\nu\sigma)]^{1/4}$ for the detachment radius r_d with $c_d = 0.3025$. The relation of Bhagat *et al.* (2018) is the same except that $c_d \simeq 0.289$ (from experiment) or $c_d = 0.277$ (from theory), later corrected by the authors to $c_d \simeq 0.2705$ (Bhagat *et al.* 2020). Using this smaller value of c_d, for the $90°$ case of figure 20(*b*),
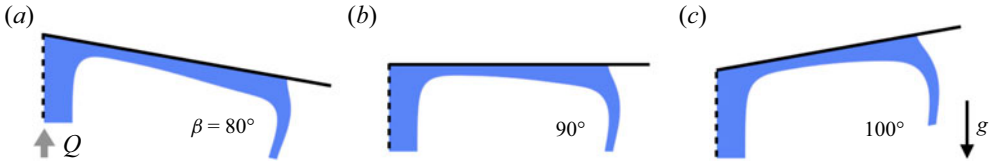
951 A20-31

Figure 20. A jet impinging from below on a conical surface angled downward (80°, panel *a*), horizontal (panel *b*) and angled upward (panel *c*, $\beta = 100°$). The contact angle with the solid surface is 90°.

the correlation gives a non-dimensional detachment radius $r_d/2a \simeq 3.823$, which is in excellent agreement with our computed value 3.825.

12. The two-dimensional case

The two-dimensional version of the present model has been described at the end of § 4. To compare with existing literature it is convenient to replace our angular coordinate β by the angle $\eta = \beta - \pi/2$, already introduced in (4.14), defined as the inclination to the horizontal. In terms of η our model becomes, upon replacing r by x,

$$\partial_t h + \partial_x q_{2D} = 0, \tag{12.1}$$

$$\partial_t q_{2D} + \frac{17}{7}\frac{q_{2D}}{h}\partial_x q_{2D} - \frac{5}{6}\left(\frac{54}{35}\frac{q_{2D}^2}{h^2} - gh\cos\eta\right)\partial_x h = \frac{5}{6}h\left(g\sin\eta + \frac{\sigma}{\rho}\partial_x\mathcal{C}\right) - \frac{5}{2}\frac{\nu q_{2D}}{h^2}. \tag{12.2}$$

As already noted, these equations coincide with those developed by Ruyer-Quil & Manneville (1998). In particular, therefore, they reproduce correctly the Kapitza stability threshold $q_{2D}/\nu = \frac{5}{6}\cot\eta$ for a flat Nusselt film (see e.g. Chang & Demekhin 2002; Kalliadasis *et al.* 2012). In the steady case, upon omitting the surface-tension contribution, (12.2) becomes

$$\left(\frac{54}{35}q_{2D}^2 - gh^3\cos\eta\right)\frac{dh}{dx} = -gh^3\sin\eta + 3\nu q_{2D}. \tag{12.3}$$

Starting from h sufficiently small, $dh/dx > 0$ and h grows. If the term in parentheses on the left-hand side approaches 0 while the right-hand side is positive, a point is reached where $dh/dx \to \infty$, which signals the presence of a hydraulic jump. The condition for this to happen is that the right-hand side be positive when $h^3 = (54/35)q_{2D}^2/(g\cos\eta)$, from which we obtain the following condition for the existence of a hydraulic jump on a two-dimensional film:

$$\cot\eta > \frac{18}{35}Re_{2D}, \tag{12.4}$$

in which $Re_{2D} = q_{2D}/\nu$ is the Reynolds number for two-dimensional film flow. The disappearance of the jump with increasing plate inclination is analogous to the disappearance of the jump with increasing β found for the cone.

A first-order model for the steady hydraulic jump in two dimensions was recently presented in Dhar *et al.* (2020). In dimensional form that result is

$$\frac{dh}{dx} = \frac{1}{K}\frac{K\nu q_{2D} - \sin\eta gh^3}{q_{2D}^2 - g\cos\eta h^3}, \tag{12.5}$$

with K a pure number dependent on the shape of the assumed velocity profile; for a parabolic profile used by Dhar *et al.* (2020) $K = \frac{5}{2}$. This expression is close to (12.3) but

951 A20-32

it cannot reproduce the condition (12.4) for the appearance of jump. A similar equation for a horizontal plate but, again, with different numerical coefficients, was given in Singha *et al.* (2005). For the related problem of a bore propagating on an inclined film, Benilov (2014) developed an approach based on the depth averaging of moments of the streamwise momentum equation. The mathematical structure of his model is different from the steady version of (12.3) in particular because it contains fourth-order spatial derivatives.

13. Summary and conclusions

The circular hydraulic jump generated by a liquid jet impinging vertically on a flat plate has been found to be easily destroyed by changing the horizontal plate to a conical surface with a downward inclination. The gravity component parallel to the surface is able to restore the liquid momentum lost to viscosity and to transform the flow to the conical analogue of the well-known two-dimensional Nusselt flow. As we have seen from the comparison of the two- and three-dimensional reduced-order models, the radial spreading of the cone surface drastically changes the mathematical nature of the problem. It may be expected that pursuing in this geometry the study of solitary waves and other wave structures analogous to those known to exist in two dimensions (see e.g. Chang & Demekhin 2002; Kalliadasis *et al.* 2012; Chakraborty *et al.* 2014) will be a challenging but very interesting undertaking.

Direct experimental evidence for the phenomena studied in the present work does not seem to be available. There is a recent paper on the circular hydraulic jump on a downward curved surface (Saberi, Mahpeykar & Teymourtash 2019) which reports an increase of the radius of the jump due to curvature. A similar trend is visible in figures 4 and 6 as the aperture of the cone is decreased and the slope of the surface correspondingly increases, but nothing more than a qualitative comparison is possible. What one may expect is that, for a given plate curvature, as the jet flow rate is increased and the jump location moves outward to a region with a sufficient slope, the jump may disappear and be replaced by the smooth increase of the thickness of the liquid layer discussed in § 7.

A final comment may be made on the possible practical and scientific implications of the present work. Liquid jets are often encountered in surface cleaning operations (see e.g. Yeckel, Middleman & Klumb 1990; Wang *et al.* 2013; Dhar *et al.* 2020) and in heat transfer (see e.g. Askarizadeh *et al.* 2020), an application in which the enhancement due to surface waves in two dimensions is amply documented (see e.g. Park *et al.* 2004; Albert, Marschall & Bothe 2014; Charogiannis & Markides 2019; Zhou & Prosperetti 2020). Other applications are encountered in the manufacturing of shells by the coating of solid bodies (see e.g. Lee *et al.* 2016) and in other coating flows (see e.g. Weinstein & Ruschak 2004; Takagi & Huppert 2010). The flow of liquid films coating the underside of a surface is of interest in the context of water bells (see e.g. Clanet 2007; Jameson *et al.* 2010), geophysics (see e.g. Takagi & Huppert 2010; Balestra *et al.* 2018; Lerisson *et al.* 2020; Ledda *et al.* 2021) and others (see e.g. Jambon-Puillet *et al.* 2021), and a conical surface is a simple geometry to study the effects of certain types of topography. Finally, some interest exists in the flow of liquid films on rotating conical surfaces (see e.g. Symons 2011; Adachi, Takahashi & Okajima 2018), a configuration to which it may be possible to extend the methods used in the present study.

Author ORCIDs.
Ⓓ Guangzhao Zhou https://orcid.org/0000-0002-9721-9628;
Ⓓ Andrea Prosperetti https://orcid.org/0000-0003-4129-7130.

Appendix A. Additional results for the first-order model

In the body of the paper we have omitted some detailed considerations so as not to interrupt the flow of the argument. We provide them here. Furthermore, there are some further results for the first-order model that are of some interest but somewhat peripheral to the main ones included in the body of the paper.

It was stated in § 7 that some discontinuous solutions of the first-order system remain for a few degrees above β_c. Figure 21 illustrates this fact. The parameters are the same as for figure 9 and, in particular, the critical angle is $\beta_c \simeq 100.52°$. Panel (*a*) is for $\beta = 101°$, just above β_c, and panel (*b*) for $\beta = 110°$. The insets show details in the neighbourhood of the critical point. In the shaded areas $\mathrm{d}\hat{h}/\mathrm{d}\hat{r} < 0$ while $\mathrm{d}\hat{h}/\mathrm{d}\hat{r} > 0$ in the white areas. Solution curves of the system (7.5), (7.6) are shown by the solid lines and exhibit a horizontal or vertical tangent as they cross the nullclines as explained in § 7. The purple line in panel (*a*) slightly overshoots the critical point and approaches it from the right, i.e. in a retrograde manner. The continuation of this branch starting at the critical point, on the other hand, has no retrograde section. In this situation, therefore, the steady first-order model does not produce a continuous solution, but only one of the two branches has a retrograde part and the gap between the two branches of the solution is typically much smaller than for $\beta < \beta_c$. In panel (*b*), on the other hand, no retrograde section is shown and the joining of the two branches of the solution is smooth. Since the film thins with increasing $\hat{r}$, for $\hat{r}$ past the critical point the relevant solution must ultimately remain in the small shaded region between the nullclines $F = 0$ and $G = 0$ to the right of the critical point. When the slope of the eigenvector corresponding to the smaller eigenvalue is non-positive, this constraint forces the line to be entirely in the region between the two nullclines and no retrograde portion is possible. When this slope is positive, the right branch of the solution curve can approach the critical point from above as shown in panel (*a*) of figure 21 and, in this case, a short retrograde portion is possible. However, as illustrated in figure 7(*b*), the slope turns negative for β very close to β_c so that this retrograde portion can only exist very close to the critical angle.

Another interesting feature of the reduced-order model (7.3) is that it possesses solutions such that the film height decreases monotonically, so that no jump can form, when it is started from initial conditions such that $\hat{h} > \hat{h}_c$ and $\hat{r} < \hat{r}_c$. Since all solutions must pass through the critical point, this situation becomes possible when, with increasing β, gravity is strong enough to balance the viscous loss of momentum. Mathematically, this transition to no-jump conditions happens for $\beta = \beta_{nj}$, the angle at which the slope of one eigenvector changes from positive to negative or, from (7.13) or (7.15), when $\partial_{\hat{r}} F = 0$. This condition, together with the criticality conditions $F = 0$, $G = 0$ leads to

$$\hat{r}_c = \frac{1}{N \cos \beta} \left(1 - \cot^2 \beta - \frac{1}{\sin \beta} \sqrt{1 + \sin^2 \beta \cot^4 \beta} \right), \tag{A1}$$

which can be substituted into (7.10) to find a relation between β_{nj} and N. As a final point it may be noted that, in principle, the eigenvalues (7.14) could be real but of opposite sign, which would make the critical point a saddle. We have verified numerically that this does not happen, at least in the range $90° \leqslant \beta \leqslant 180°$, $10^{-3} \leqslant N \leqslant 10^3$.
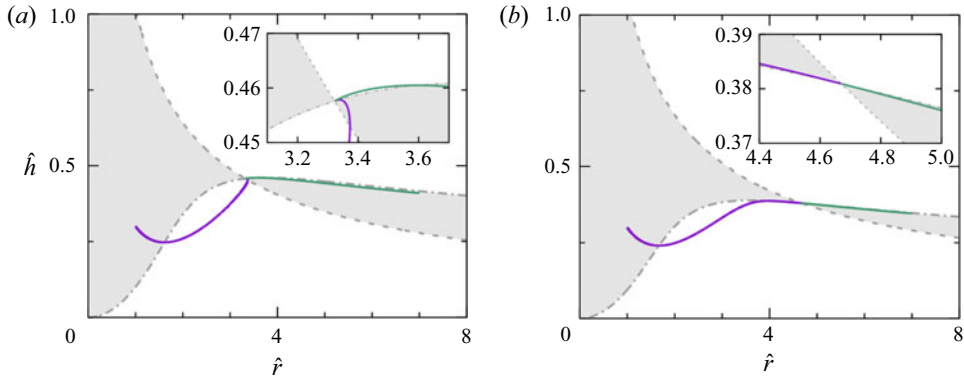
Figure 21. Examples of solutions of the first-order model (7.5), (7.6) near (panel (*a*), for $\beta = 101°$) and farther from (panel (*b*), for $\beta = 110°$) the critical angle $\beta_c = 100.52°$. The insets show enlargements in the neighbourhood of the critical point; $d\hat{h}/d\hat{r} < 0$ in the shaded areas while $d\hat{h}/d\hat{r} > 0$ in the white areas.

Appendix B. Liquid film flow on the surface of a vertical cylinder

The reduced-order model (2.8), (4.10) can be adapted to describe the axisymmetric flow of a liquid film down the surface of a vertical cylinder with radius $R \gg h$ by taking the limit $\beta \to \pi$ and $r \to \infty$ with $r \sin \beta \to R$; if the z axis is taken directed downward we can replace ∂_r by ∂_z. With these transformations, the mass conservation equation (2.8) becomes

$$\partial_t h + \frac{1}{R+h} \partial_z q = 0. \tag{B1}$$

(The analogue to the form (4.9) can be obtained by replacing the factor $(R+h)^{-1}$ by its Taylor series expansion $R^{-1} - hR^{-2}$.) Equation (4.10) for q becomes instead

$$\partial_t q + \frac{17}{7} \frac{q}{hR} \partial_z q - \frac{9}{7} \frac{q^2}{Rh^2} \partial_z h = \frac{5}{6} Rh \left(g + \frac{\sigma}{\rho} \partial_z \mathcal{C} \right) - \frac{5}{2} \frac{\nu q}{h^2} \left(1 - \frac{h}{R} \right), \tag{B2}$$

which coincides with the result given in Ruyer-Quil *et al.* (2008) in the limit $h/R \ll 1$. The curvature (3.21) is

$$\mathcal{C} \simeq -\frac{1}{R+h} + \partial_z^2 h \simeq -\frac{1}{R} + \frac{h}{R^2} + \partial_z^2 h. \tag{B3}$$

Appendix C. Numerical aspects

The solver interIsoFoam implemented in the open-source software OpenFOAM v2012 was used for the Navier–Stokes equations. The incompressible form of the equations is solved in a finite-volume framework with the PISO method (pressure implicit with splitting of operators, Issa 1986). The volume-of-fluid method is used to describe the evolution of the two immiscible fluids (gas and liquid), with the surface-tension effect evaluated by using a continuum surface force model (Brackbill, Kothe & Zemach 1992). The interface between the two phases is captured by using the isoAdvector approach (Roenby, Bredmose & Jasak 2016). The flow field is updated in time with a first-order implicit Euler scheme. The second-order linear-upwind scheme is used for spatial discretization of the Navier–Stokes equations, whereas a van Leer limiter is applied to the phase-fraction field.
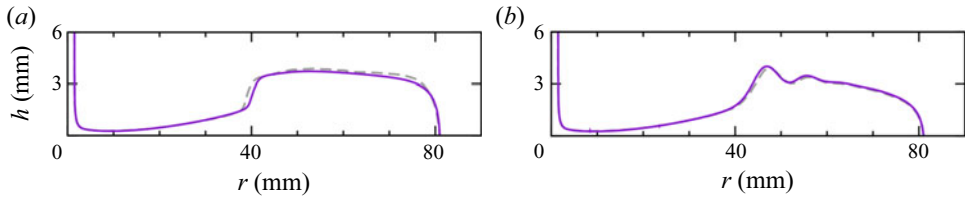
Figure 22. Comparison of our NS results (purple solid lines) with those of Fernandez-Feria *et al.* (2019), with (left) and without (right) surface tension effects.

In most cases shown in this paper, we use a uniform mesh with the cell aspect ratio close to 1. For very long domains the length of which is, e.g. over 30 times greater than the height, nonuniform meshes were carefully generated for a better computational efficiency while ensuring that the wall region and the hydraulic-jump region are accurately resolved.

The computational domain is initially full of a medium ('gas') with density and viscosity three orders of magnitude smaller than those of the liquid. The jet is injected from the inlet with a uniform velocity profile. For all wall boundaries we use no-slip conditions. At the outlet of the liquid, the flow is essentially fully developed and therefore we can fix the static pressure to a reference value; for the velocity we use a standard outlet condition, i.e. the velocity gradient normal to the boundary is taken to vanish. At the boundary of the gas domain, the total pressure (static plus dynamic) is fixed and the gas can freely enter or exit the domain from there. We tried different options finding negligible differences due to the small density and viscosity of the gas.

In the presence of a contact line, the liquid–solid contact angle is set to be $90°$. It was found that, in a few cases, small bubbles might be trapped in the film during the initial transient in which the liquid film rapidly spreads. To avoid the possibility of an effect on the local shape of the gas–liquid interface, we artificially remove these bubbles and then continue the simulation until it finally reaches a steady state.

Standard grid-convergence tests have been conducted for typical cases. The computational mesh was continuously doubled until the shape of the free-surface distribution was no longer affected by the mesh refinement. The results reported in this paper are all obtained with the finest meshes.

As a last test case further confirming the accuracy of our numerical method we show in figure 22 a comparison of our predictions (solid lines) with the numerical results from figure 6(*a*) (WG30/70) of Fernandez-Feria *et al.* (2019) (dashed lines) with (left) and without (right) surface tension.

For the solution of the time-dependent reduced-order model (8.1) we used the method of lines. The partial differential equations are converted into a system of ordinary differential equations in time by approximating all spatial derivatives with central finite differences on a uniform grid. The resulting system is then solved with the aforementioned Bogacki–Shampine method. Since the system is hyperbolic, central difference discretization leads to an unstable scheme. In order to stabilize the computation and suppress possible unphysical oscillations, we adapt the concept underlying the design of the Jameson–Schmidt–Turkel scheme (Jameson, Schmidt & Turkel 1981) adding necessary artificial dissipation in both the equations for h and q. In detail, the original equation at the spatial node j, synthetically written in the form

$$\partial_t w_j = \mathcal{R}_j(h, q), \tag{C1}$$

with w representing either h or q, is approximated as

$$\partial_t w_j = \mathcal{R}'_j = \mathcal{R}_j + \Lambda_j \Delta r \left[\epsilon_j^{(2)} \left[\partial_r^2 w \right]_j - \epsilon_j^{(4)} \Delta r^2 \left[\partial_r^4 w \right]_j \right], \tag{C2}$$

where Δr is the grid size and $\Lambda_j = \max(\lambda_{+,j-1}, \lambda_{+,j}, \lambda_{+,j+1})$ with λ_+ given by (8.4). The fourth-order derivative serves as a background dissipation term dampening high-frequency components, whereas the second-order one takes care of strong discontinuities. The coefficients are calculated according to

$$\epsilon_j^{(2)} = \kappa^{(2)} \max\left(f_{j-1}, f_j, f_{j+1} \right), \quad \epsilon_j^{(4)} = \max\left[0, \kappa^{(4)} - \epsilon_j^{(2)} \right]. \tag{C3a,b}$$

The sensor for discontinuity f_j is expressed as

$$f_j = \frac{|h_{j+1} - 2h_j + h_{j-1}|}{\max\left(|h_{j+1} - h_j| + |h_j - h_{j-1}|, \delta_{lim} \right)}, \tag{C4}$$

where δ_{lim} is a small parameter that prevents the denominator from vanishing when the film thickness h is locally constant. Our numerical tests show that the values of the empirical constants $\kappa^{(2)} = \frac{1}{2}$, $\kappa^{(4)} = \frac{1}{64}$ maintain a good balance between accuracy and the need for numerical stability. It should be mentioned that, due to the extra terms added to the h equation, the flow rate q exhibits a spike in a small region encompassing the jump, after which it settles to a value slightly different from that ahead of the jump. This effect is most significant for the 90-degree case we have tested, the relative difference in q across the hydraulic jump being approximately 3.4 %. This error becomes much smaller, 0.2 %, for the 95-degree case where the hydraulic jump is milder. In any case, there is no evidence that this discrepancy causes significant mismatch in terms of the film thickness compared with the Navier–Stokes simulations as can be seen e.g. in figure 13. That being said, there is potential for the present numerical method to be improved to avoid these artefacts and yield more accurate results, especially in consideration of the variety of techniques for numerical treatment of shock waves in compressible fluid dynamics to which the hydraulic jump phenomenon exhibits several similarities (see Kasimov 2008).

For the reverse-gravity examples of § 11 there is a region of the (h, r) plane where the eigenvalues (8.4) are complex. In these regions the smoothing procedure described above is unnecessary.

REFERENCES

ADACHI, T., TAKAHASHI, Y. & OKAJIMA, J. 2018 Film flow thickness along the outer surface of rotating cones. *Eur. J. Mech.* (B/*Fluids*) **68**, 39–44.

AL-HAWAJ, O. 1999 A numerical study of the hydrodynamics of a falling liquid film on the internal surface of a downward tapered cone. *Chem. Engng J.* **75**, 177–182.

ALBERT, C., MARSCHALL, H. & BOTHE, D. 2014 Direct numerical simulation of interfacial mass transfer into falling films. *Intl J. Heat Mass Transfer* **69**, 343–357.

ASKARIZADEH, H., AHMADIKIA, H., EHRENPREIS, C., KNEER, R., PISHEVAR, A. & ROHLFS, W. 2019 Role of gravity and capillary waves in the origin of circular hydraulic jumps. *Phys. Rev. Fluids* **4**, 114002.

ASKARIZADEH, H., AHMADIKIA, H., EHRENPREIS, C., KNEER, R., PISHEVAR, A. & ROHLFS, W. 2020 Heat transfer in the hydraulic jump region of circular free-surface liquid jets. *Intl J. Heat Mass Transfer* **146**, 118823.

BALESTRA, G., NGUYEN, D.M.-P. & GALLAIRE, F. 2018 Rayleigh–Taylor instability under a spherical substrate. *Phys. Rev. Fluids* **3**, 084005.

BENILOV, E.S.. 2014 Depth-averaged model for hydraulic jumps on an inclined plate. *Phys. Rev.* **E89**, 053013.

BHAGAT, R.K., JHA, N.K., LINDEN, P.F. & WILSON, D.I. 2018 On the origin of the circular hydraulic jump in a thin liquid film. *J. Fluid Mech.* **851**, R5.

BHAGAT, R.K. & LINDEN, P.F. 2020 The circular capillary jump. *J. Fluid Mech.* **896**, A25.

BHAGAT, R.K., WILSON, I.D. & LINDEN, P.F. 2020 Experimental evidence for surface tension origin of the circular hydraulic jump. arXiv:2010.04107v3.

BOGACKI, P. & SHAMPINE, L.F. 1989 A 3(2) pair of Runge–Kutta formulas. *Appl. Maths Lett.* **2**, 321–325.

BOHR, T., DIMON, P. & PUTKARADZE, V. 1993 Shallow-water approach to the circular hydraulic jump. *J. Fluid Mech.* **254**, 635–648.

BOHR, T., ELLEGAARD, C., ESPE HANSEN, A., HANSEN, K., HAANING, A., PUTKARADZE, V. & WATANABE, S. 1998 Separation and pattern formation in hydraulic jumps. *Physica* A **249**, 111–117.

BOHR, T., ELLEGAARD, C., HANSEN, A.E. & HAANING, A. 1996 Hydraulic jumps, flow separation and wave breaking: an experimental study. *Physica* B **228**, 1–10.

BOHR, T., PUTKARADZE, V. & WATANABE, S. 1997 Averaging theory for the structure of hydraulic jumps and separation in laminar free-surface flows. *Phys. Rev. Lett.* **79**, 1038–1041.

BRACKBILL, J.U., KOTHE, D.B. & ZEMACH, C. 1992 A continuum method for modeling surface tension. *J. Comput. Phys.* **100**, 335–354.

BRECHET, Y. & NÉDA, Z. 1999 On the circular hydraulic jump. *Am. J. Phys.* **67**, 723–731.

BRUN, P.-T., DAMIANO, A., RIEU, P., BALESTRA, G. & GALLAIRE, F. 2015 Rayleigh–Taylor instability under an inclined plane. *Phys. Fluids* **27**, 084107.

BUSH, J.W.M. & ARISTOFF, J.M. 2003 The influence of surface tension on the circular hydraulic jump. *J. Fluid Mech.* **489**, 229–238.

BUTTON, E.C., DAVIDSON, J.F., JAMESON, G.J. & SADER, J.E. 2010 Water bells formed on the underside of a horizontal plate. Part 2. Theory. *J. Fluid Mech.* **649**, 45–68.

CHAKRABORTY, S., NGUYEN, P.-K., RUYER-QUIL, C. & BONTOZOGLOU, V. 2014 Extreme solitary waves on falling liquid films. *J. Fluid Mech.* **745**, 564–591.

CHANG, H.-C. & DEMEKHIN, E.A. 2002 *Complex Wave Dynamics on Thin Films*. Elsevier.

CHAROGIANNIS, A. & MARKIDES, C.N. 2019 Spatiotemporally resolved heat transfer measurements in falling liquid-films by simultaneous application of planar laser-induced fluorescence (PLIF), particle tracking velocimetry (PTV) and infrared (IR) thermography. *Exp. Therm. Fluid Sci.* **107**, 169–191.

CLANET, C. 2007 Waterbells and liquid sheets. *Annu. Rev. Fluid Mech.* **39**, 469–496.

DASGUPTA, R. & GOVINDARAJAN, R. 2010 Nonsimilar solutions of the viscous shallow water equations governing weak hydraulic jumps. *Phys. Fluids* **22**, 112108.

DASGUPTA, R., TOMAR, G. & GOVINDARAJAN, R. 2015 Numerical study of laminar, standing hydraulic jumps in a planar geometry. *Eur. Phys. J.* E **38**, 45.

DE VITA, F., LAGRÉE, P.-Y., CHIBBARO, S. & POPINET, S. 2020 Beyond shallow water: appraisal of a numerical approach to hydraulic jumps based upon the boundary layer theory. *Eur. J. Mech. (*B*/Fluids)* **79**, 233–246.

DHAR, M., DAS, G. & DAS, P.K. 2020 Planar hydraulic jumps in thin film flow. *J. Fluid Mech.* **884**, A11.

DING, Z. & WONG, T.N. 2017 Three-dimensional dynamics of thin liquid films on vertical cylinders with Marangoni effect. *Phys. Fluids* **29**, 011701.

DUCHESNE, A., ANDERSEN, A. & BOHR, T. 2019 Surface tension and the origin of the circular hydraulic jump in a thin liquid film. *Phys. Rev. Fluids* **4**, 084001.

DUCHESNE, A., LEBON, L. & LIMAT, L. 2014 Constant Froude number in a circular hydraulic jump and its implication on the jump radius selection. *Europhys. Lett.* **107**, 54002.

DUCHESNE, A. & LIMAT, L. 2022 Circular hydraulic jumps: where does surface tension matter? *J. Fluid Mech.* **937**, R2.

FERNANDEZ-FERIA, R., SANMIGUEL-ROJAS, E. & BENILOV, E.S. 2019 On the origin and structure of a stationary circular hydraulic jump. *Phys. Fluids* **31**, 072104.

FRENKEL, A.L. 1992 Nonlinear theory of strongly undulating thin films flowing down vertical cylinders. *Europhys. Lett.* **18**, 583–588.

GLENDINNING, P. 1994 *Stability, Instability and Chaos*. Cambridge University Press.

HANSEN, S.H., HØRLÜCK, S., ZAUNER, D., DIMON, P., ELLEGAARD, C. & CREAGH, S.C. 1997 Geometric orbits of surface waves from a circular hydraulic jump. *Phys. Rev.* E **55**, 7048–7061.

HIGUERA, F.J. 1994 The hydraulic jump in a viscous laminar flow. *J. Fluid Mech.* **274**, 69–92.

INDEIKINA, A., VERETENNIKOV, I. & CHANG, H.-C. 1997 Drop fall-off from pendent rivulets. *J. Fluid Mech.* **338**, 173–201.

ISSA, R.I. 1986 Solution of the implicitly discretised fluid flow equations by operator-splitting. *J. Comput. Phys.* **62**, 40–65.

JAMBON-PUILLET, E., LEDDA, P.G., GALLAIRE, F. & BRUN, P.-T. 2021 Drops on the underside of a slightly inclined wet substrate move too fast to grow. *Phys. Rev. Lett.* **127**, 044503.

JAMESON, A., SCHMIDT, W. & TURKEL, E. 1981 Numerical solution of the Euler equations by finite volume methods using Runge Kutta time stepping schemes. *AIAA 14th Fluid and Plasma Dynamics Conference, Palo Alto CA. AIAA Paper* 81-1259.

JAMESON, G.J., JENKINS, C.E., BUTTON, E.C. & SADER, J.E. 2010 Water bells formed on the underside of a horizontal plate. Part 1. Experimental investigation. *J. Fluid Mech.* **649**, 19–43.

JI, H., FALCON, C., SADEGHPOUR, A., ZENG, Z., JU, Y.S. & BERTOZZI, A.L. 2019 Dynamics of thin liquid films on vertical cylindrical fibres. *J. Fluid Mech.* **865**, 303–327.

KALLIADASIS, S. & CHANG, H.-C. 1994 Drop formation during coating of vertical fibres. *J. Fluid Mech.* **261**, 135–168.

KALLIADASIS, S., RUYER-QUIL, C., SCHEID, B. & VELARDE, M.G. 2012 *Falling Liquid Films*. Springer.

KASIMOV, A.R. 2008 A stationary circular hydraulic jump, the limits of its existence and its gasdynamic analogue. *J. Fluid Mech.* **601**, 189–198.

KOFMAN, N., ROHLFS, W., GALLAIRE, F., SCHEID, B. & RUYER-QUIL, C. 2018 Prediction of two-dimensional dripping onset of a liquid film under an inclined plane. *Intl J. Multiphase Flow* **104**, 286–293.

KURIHARA, M. 1946 Laminar flow in a horizontal liquid layer. Report of the Research Institute for Fluid Engineering, Kyusyu Imperial University, vol. 3, pp. 11–33.

LAGERSTROM, P.A. & CASTEN, R.G. 1972 Basic concepts underlying singular perturbation techniques. *SIAM Rev.* **14**, 63–120.

LEAL, L.G. 2007 *Advanced Transport Phenomena*. Cambridge University Press.

LEDDA, P.G., BALESTRA, G., LERISSON, G., SCHEID, B., WYART, M. & GALLAIRE, F. 2021 Hydrodynamic-driven morphogenesis of karst draperies: spatio-temporal analysis of the two-dimensional impulse response. *J. Fluid Mech.* **910**, A53.

LEE, A., BRUN, P.-T., MARTHELOT, J., BALESTRA, G., GALLAIRE, F. & REIS, P.M. 2016 Fabrication of slender elastic shells by the coating of curved surfaces. *Nat. Commun.* **7**, 11155.

LEFSCHETZ, S. 1963 *Differential Equations: Geometric Theory*, 2nd edn. Interscience Publishers, reprinted by Dover, New York, 1977.

LERISSON, G., LEDDA, P.G., BALESTRA, G. & GALLAIRE, F. 2020 Instability of a thin viscous film flowing under an inclined substrate: steady patterns. *J. Fluid Mech.* **898**, A6.

LIN, T.-S., DIJKSMAN, J.A. & KONDIC, L. 2021 Thin liquid films in a funnel. *J. Fluid Mech.* **924**, A26.

MATHUR, M., DASGUPTA, R., SELVI, N.R., JOHN, N.S., KULKARNI, G.U. & GOVINDARAJAN, R. 2007 Gravity-free hydraulic jumps and metal femtoliter cups. *Phys. Rev. Lett.* **98**, 164502.

MOHAJER, B. & LI, R. 2015 Circular hydraulic jump on finite surfaces with capillary limit. *Phys. Fluids* **27**, 117102.

ORON, A., DAVIS, S.H. & BANKOFF, S.G. 1997 Long-scale evolution of thin liquid films. *Revs. Mod. Phys.* **69**, 931–980.

PARK, C.D., NOSOKO, T., GIMA, S. & RO, S.T. 2004 Wave-augmented mass transfer in a liquid film falling inside a vertical tube. *Intl J. Heat Mass Transfer* **47**, 2587–2598.

ROENBY, J., BREDMOSE, H. & JASAK, H. 2016 A computational method for sharp interface advection. *Roy. Soc. Open Sci.* **3**, 160405.

ROJAS, N., ARGENTINA, M. & TIRAPEGUI, E. 2013 A progressive correction to the circular hydraulic jump scaling. *Phys. Fluids* **25**, 042105.

ROJAS, N.O., ARGENTINA, M., CERDA, E. & TIRAPEGUI, E. 2010 Inertial lubrication theory. *Phys. Rev. Lett.* **104**, 187801.

RUYER-QUIL, C. & MANNEVILLE, P. 1998 Modeling film flows down inclined planes. *Eur. Phys. J.* B **6**, 227–292.

RUYER-QUIL, C. & MANNEVILLE, P. 2000 Improved modeling of flows down inclined planes. *Eur. Phys. J.* B **15**, 357–369.

RUYER-QUIL, C., TREVELEYAN, P., GIORGIUTTI-DAUPHINÉ, F., DUPRAT, C. & KALLIADASIS, S. 2008 Modelling film flows down a fibre. *J. Fluid Mech.* **603**, 431–462.

SABERI, A., MAHPEYKAR, M.R. & TEYMOURTASH, A.R. 2019 Experimental measurement of radius of circular hydraulic jumps: effect of radius of convex target plate. *Flow Meas. Instrum.* **65**, 274–279.

SCHOLLE, M., MARNER, F. & GASKELL, P.H. 2019 Thin liquid film formation on hemispherical and conical substrate. *Proc. Appl. Maths Mech.* **19**, e201900111.

SINGHA, S.B., BHATTACHARJEE, J.K. & RAY, A.K. 2005 Hydraulic jump in one-dimensional flow. *Eur. Phys. J.* B **48**, 417–426.

STROGATZ, S.H. 2015 *Nonlinear Dynamics and Chaos*, 2nd edn. Perseus Books.

SYMONS, D.D. 2011 Integral methods for flow in a conical centrifuge. *Chem. Engng Sci.* **66**, 3020–3029.

TAKAGI, D. & HUPPERT, H.E. 2010 Flow and instability of thin films on a cylinder and sphere. *J. Fluid Mech.* **647**, 221–238.

TANI, I. 1949 Water jump in the boundary layer. *J. Phys. Soc. Japan* **4**, 212–215.

WANG, T., FARIA, D., STEVENS, L.J., TAN, J.S.C., DAVIDSON, J.F & WILSON, D.I. 2013 Flow patterns and draining films created by horizontal and inclined coherent water jets impinging on vertical walls. *Chem. Engng Sci.* **102**, 585–601.

WANG, Y. & KHAYAT, R.E. 2019 The role of gravity in the prediction of the circular hydraulic jump radius for high-viscosity liquids. *J. Fluid Mech.* **862**, 128–161.

WANG, Y. & KHAYAT, R.E. 2021 The effects of gravity and surface tension on the circular hydraulic jump for low- and high-viscosity liquids: a numerical investigation. *Phys. Fluids* **33**, 012105.

WATANABE, S., PUTKARADZE, V. & BOHR, T. 2003 Integral methods for shallow free-surface flows with separation. *J. Fluid Mech.* **480**, 233–265.

WATSON, E.J. 1964 The radial spread of a liquid jet over a horizontal plate. *J. Fluid Mech.* **20**, 481–499.

WEINSTEIN, S.J. & RUSCHAK, K.J. 2004 Coating flows. *Annu. Rev. Fluid Mech.* **36**, 29–53.

XUE, N. & STONE, H.A. 2021 Draining and spreading along geometries that cause converging flows: viscous gravity currents on a downward-pointing cone and a bowl-shaped hemisphere. *Phys. Rev. Fluids* **6**, 043801.

YECKEL, A., MIDDLEMAN, S. & KLUMB, L.A. 1990 The removal of thin liquid films from periodically grooved surfaces by an impinging jet. *Chem. Engng Commun.* **96**, 69–79.

YIANTSIOS, S.G. & HIGGINS, B.G. 1989 Rayleigh–Taylor instability in thin viscous films. *Phys. Fluids* **A1**, 1484–1501.

ZHOU, G. & PROSPERETTI, A. 2020 A numerical study of mass transfer from laminar liquid films. *J. Fluid Mech.* **902**, A10.

ZHOU, G. & PROSPERETTI, A. 2022 Dripping instability of a two-dimensional liquid film under an inclined plate. *J. Fluid Mech.* **932**, A49.

ZOLLARS, R.L. & KRANTZ, W.B. 1976 Laminar film flow down a right circular cone. *Ind. Engng Chem. Fundam.* **15**, 91–94.

ZOLLARS, R.L. & KRANTZ, W.B. 1980 Non-parallel flow effects on the stability of film flow down a right circular cone. *J. Fluid Mech.* **96**, 585–601.